Universities of Leeds, Sheffield and York
http://eprints.whiterose.ac.uk/

A Numerical Investigation into the Influence of Unsteady Wind in the Performance of a Vertical Axis Wind Turbine

Louis Angelo Danao[1], Okeoghene Eboibi[2], Robert Howell[3]
Department of Mechanical Engineering
University of Sheffield, Sheffield S1 3JD, U.K

Abstract

Lorem ipsum dolor sit amet, consectetur adipiscing elit. Phasellus lacus elit, accumsan vitae vestibulum sit amet, mollis et dui. Nulla est leo, viverra at rhoncus at, mollis sit amet odio. Donec consectetur, velit sit amet fringilla blandit, sem libero cursus tellus, ac luctus lacus turpis at nunc. In lacus urna, ultricies nec convallis vel, iaculis vel lacus. Praesent porta erat id mauris pellentesque imperdiet. Maecenas et diam et dui vehicula blandit pulvinar in dui. Aenean mattis erat eget turpis tincidunt hendrerit. Suspendisse potenti. Pellentesque quis odio non sem auctor interdum. Duis rhoncus egestas augue, vel venenatis orci scelerisque et. Nulla risus felis, dictum nec congue et, eleifend id dolor. Mauris ac tortor vulputate lorem tincidunt tincidunt. Vivamus vestibulum sagittis lacus vel feugiat. Mauris ac odio ut diam dignissim venenatis. Cum sociis natoque penatibus et magnis dis parturient montes, nascetur ridiculus mus. Suspendisse potenti.

I. Introduction

A general consensus has been made in the recent years that the effects of climate change are becoming more severe and prevalent [1]. The main cause of the increasing rate of undesirable climatic conditions has been identified as greenhouse gas emissions from the burning of fossil fuels used primarily for energy generation and transportation purposes. For this reason, there has been a pressing need to reduce emissions through the use of technologies that are capable of extracting energy from the environment whilst being non–polluting and sustainable. Several alternative sources to fossil fuels have been identified: tidal, solar, biomass, and wind. These are branded as 'renewables' and have attracted significant research attention in the past decades. Of these renewable sources, the contribution of wind to the total energy generation of the U.K. has been steadily rising over the last few years and has seen the greatest increase in 2011 of 68% for offshore installations and 45% for onshore [2]. Wind has also been the leading renewable technology for electricity generation with 45% of the total 2011 renewable production. Despite these numbers, the total consumption of electricity from renewable sources only account for 9.4%. And the proportion of wind in the overall consumption is very low at 0.7% [3]. As a result, further research is needed to increase the understanding of this renewable power source to promote its wider adoption.

---

[1] PhD Student, University of Sheffield; Assistant Professor, University of the Philippines.
[2] PhD Student, University of Sheffield; Lecturer, Delta State Polytechnic, Nigeria.
[3] Lecturer in Experimental Aerodynamics, University of Sheffield.

So much of the work on VAWT research is focused on steady wind conditions. If their use in the built environment is to be successful, current efforts related to small scale VAWT should concentrate more on unsteady wind performance since the wind in the urban terrain is never steady, which makes all of the steady wind analyses of less use. The accurate assessment of the effects of unsteady wind to the performance of the VAWT poses a significant challenge. The present literature on numerical simulations of VAWTs subjected to unsteady wind is very limited and majority use mathematical models that derive blade forces from table lookups of static aerofoil data. High resolution Navier–Stokes based Computational Fluid Dynamics (CFD) models that are independent of such tables barely exist.

It is the aim of the present work to fill in the gaps in the literature and provide a substantial knowledgebase on numerical methods, data and analyses that will increase the current understanding of VAWT performance to include not just steady wind conditions but also fluctuating winds that are characteristic of the built environment. The research described in this study includes the development of a CFD–based numerical model, presented and validated against experiments to aid in the analysis of how and why a VAWT performs as it does in unsteady wind. The crucial linking of aerodynamics and performance is a key point in this body of work which will provide a more complete picture of VAWT operation in unsteady wind.

II. CFD Solver

The CFD package, Ansys Fluent 13.0, was used for all the simulations performed in this study. The code uses the finite volume method to solve the governing equations for fluids. More specifically in this project the incompressible, unsteady Reynolds Averaged Navier–Stokes (URANS) equations are solved for the entire flow domain. The coupled pressure–based solver was selected with a second order implicit transient formulation for improved accuracy. All solution variables were solved via second order upwind discretisation scheme since most of the flow can be assumed to be not in line with the mesh [4].
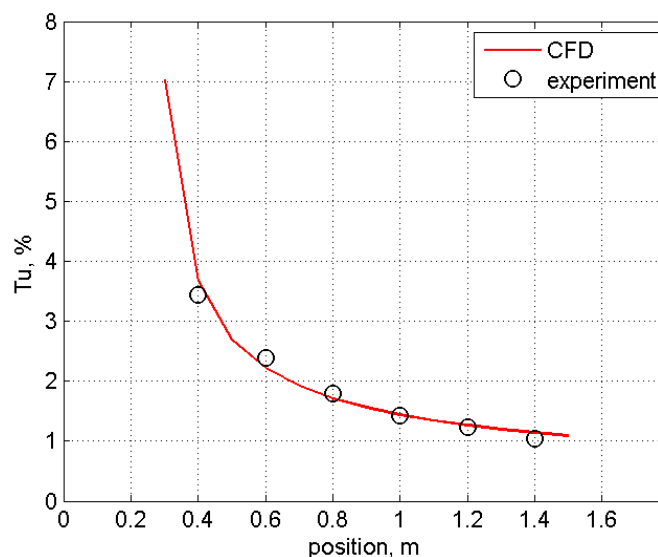
Figure 1. Comparison of turbulent intensity decay between CFD and experiments
(x = 0: test section inlet).

The entire domain was initialised using the inlet conditions that were pre–determined to provide a matching turbulence intensity decay that was observed in VAWT experiments conducted in the University of Sheffield wind tunnel facility. The inlet turbulence intensity was set to Tu = 8% with a turbulence viscosity ratio of $\mu_t/\mu = 14$. The Tu decay in the numerical model is very close to the observed decay in the experiment as shown in Figure 1.

III. Numerical Model of the Wind Tunnel VAWT

A two–dimensional CFD model was used to represent the VAWT and the wind tunnel domain. This was based on the review of relevant literature [5-17] that has shown that a 2D model is sufficient in revealing the factors that influence the performance and majority of flow physics that surround the VAWT. The contributions of blade end effects and blade–support arm junction effects are neglected but deemed acceptable since these can be considered as secondary. Two dimensional VAWT models are essentially VAWTs with infinite aspect ratio blades. The effect of blade aspect ratio (AR) comes in the form of shifting the CP curve upwards and to the right as AR increases [18], but the general shape is maintained. Full 3D models were tested using coarse meshes but due to their immense computational time requirements, were eventually shelved. The complexity, as well as the computational expense for a full three dimensional model cannot be justified by the additional insight that such a model can offer and is left for future work.
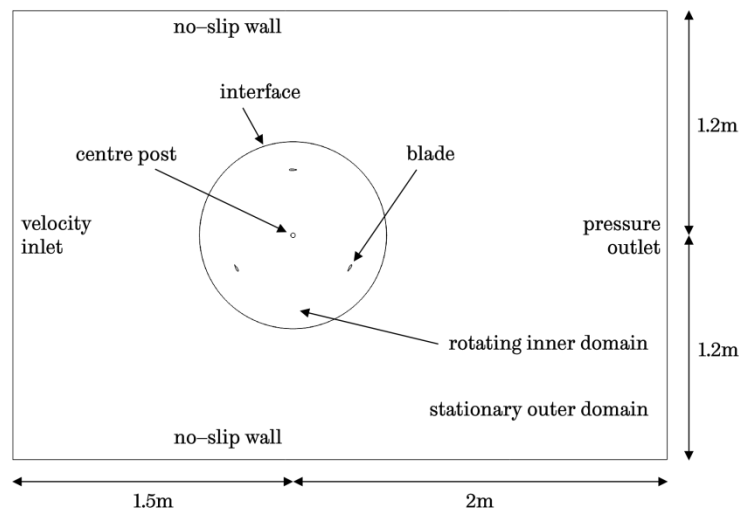
Figure 2. An illustration of the 2D numerical domain.

The domain mesh was created where the aerofoil coordinates of a NACA022 profile were imported to define the blade shape. The surrounding geometry was defined based on studies of the extents of the boundaries that are detailed in later sections. There is an inner circular rotating domain connected to a stationary rectangular domain via a sliding interface boundary condition that conserves both mass and momentum. No–slip boundaries are set to represent the wind tunnel walls while a velocity inlet and a pressure outlet are used for the test section inlet and outlet, respectively. The rotation of the inner domain relative to the outer domain is prescribed within the solver that implements the algorithm for the sliding mesh technique.

Care is taken such that tolerance between meshes in the interface region is kept low to avoid excessive numerical diffusion.

Each blade surface was meshed with 300 nodes and clustering in the leading and trailing edges was implemented to provide the required refinement in regions where high gradients in pressure and flow were expected. A node density study was performed to determine the appropriate number of surface nodes (Figure 3). The O–type mesh was adapted for the model, where a boundary layer was inflated from the blade surface (Figure 4). The motivation behind using the O–type mesh instead of the conventional C–type used in aerofoil studies was primarily because the expected wake is not fixed on a specific path relative to the blade but rather varying greatly in direction swaying from one side to another side. The use of a C–type mesh would not be beneficial as the tail of the wake from the blade will not always fall within the refined tail mesh. The first cell height used was such that the y^+ values from the flow solutions did not exceed 1, the limit of the turbulence model that was chosen for the simulations. To ensure proper boundary layer modelling, the growth rate of the inflation was set to 1.1 to give a minimum of 30 layers within the boundary layer, after which a larger growth rate of 1.15 was implemented. Beyond the blade surface of about a chord width, the rotating inner domain mesh was generated such that the maximum edge length of the cells did not exceed 0.5c within the VAWT domain (Figure 5). This was adapted to minimise the dissipation of the turbulent structures generated by the blades in the upwind region that may interact with the other blades in downwind region. A smoothing algorithm in the meshing software was used to reduce the angle skewness of the cells such that the maximum was observed to be less than 0.6.
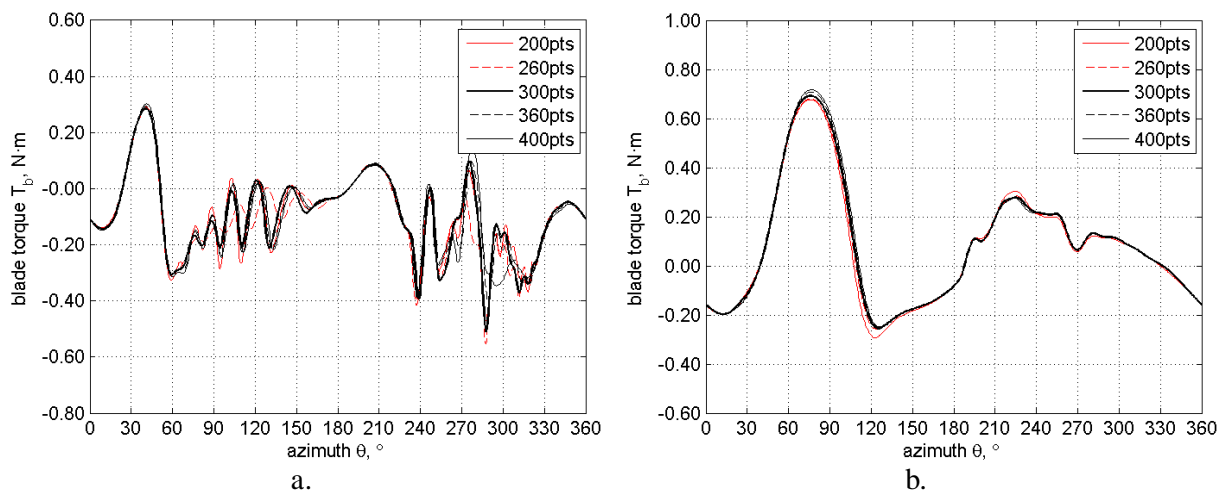
Figure 3. Blade torque for node density study: a) $\lambda = 2$, b) $\lambda = 4$.
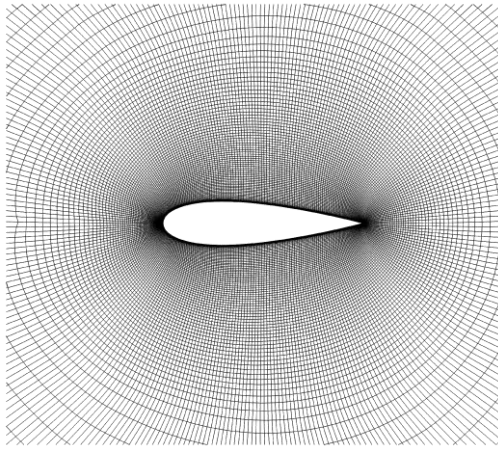
Figure 4. The near–blade mesh
of the numerical model.
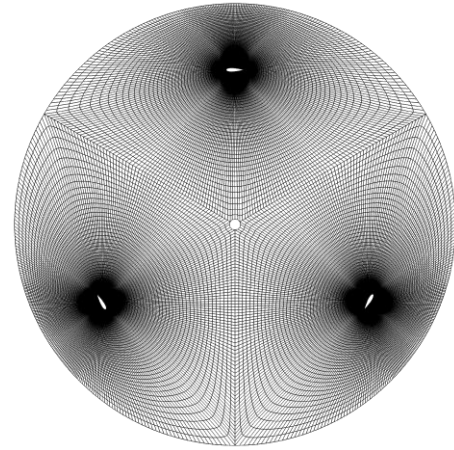
Figure 5. The rotating inner domain mesh
of the numerical model.

To reduce computation time, the outer domain was coarsely meshed with a rough maximum edge length of the cells set to c (Figure 6). This dissipated the high gradients in the wake, such as shed vortices, but the general velocity deficit was still captured. The distance of the velocity inlet boundary from the VAWT axis was set to 1.5m, 0.3m short of the actual 1.8m in the experiment setup. This was not considered an issue since the modelled turbulence intensity decay in the simulations matched that of the experiments and is thought to be much more important.
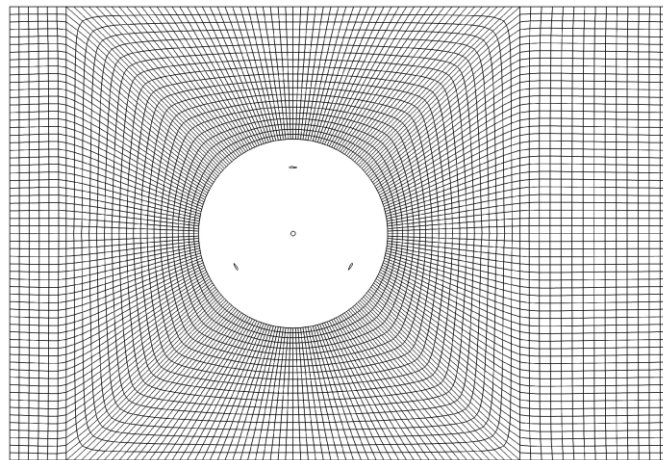
Figure 6. The stationary outer domain mesh of the numerical model.

An outlet distance study was conducted to investigate the effects of wake development on the performance of the VAWT (Figure 7a). The pressure outlet boundary was set to $d_o = 2m$ from the VAWT axis. This has been selected as a distance between the actual test section outlet of 1.2m and the position of the wind tunnel fan of about 3m. In the actual wind tunnel setup, the test section outlet was fitted with a steel matting grid of the same wire thickness and mesh size as the turbulence grid in the inlet. This will have had a definite effect on the developed wake of the VAWT, breaking up the large vortex structures generated from the blades. There is also the presence of the shutter flaps, that is considered to influence the destruction of the shed vortices. As such, a long fluid domain behind the VAWT was deemed unnecessary from a numerical standpoint since full wake development was not one of the objectives of the study.

A wall distance study was carried out to examine the effects of blockage in the 2D simulations (Figure 7b). The side wall distance was set to $d_s = 1.2$m from the VAWT axis. This is double the actual wind tunnel wall distance of 0.6m. The blockage of the 2D numerical model matches that of the 3D wind tunnel model and is equal to 0.29. Since the study is mainly focused on the aerodynamics of the VAWT in unsteady wind conditions within a wind tunnel domain, blockage was not a primary consideration in the simulations since no reference to actual field test data is made.

a.   b.
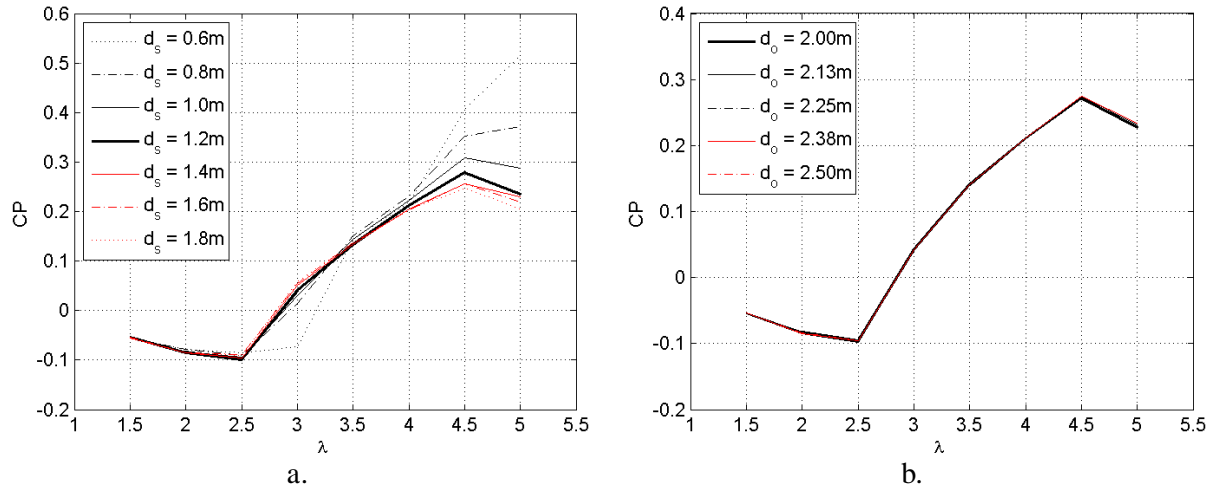
Figure 7. Domain size study results for the 2D numerical model:
a) side wall distance, b) domain length.

Time step convergence was monitored for all conserved variables and it was observed that acceptable levels of residuals (less than 1×10^{-6}) were attained after 6 rotations of the VAWT. This meant that periodic convergence was also achieved. The blade torque T_b monitored all though 10 rotations is shown in Figure 8. After the sixth rotation, the peaks of the upwind torque for cycles 7 through 10 are level and the downwind ripple match closely. The difference in average torque between cycle 7 and cycle 10 is around 0.5%
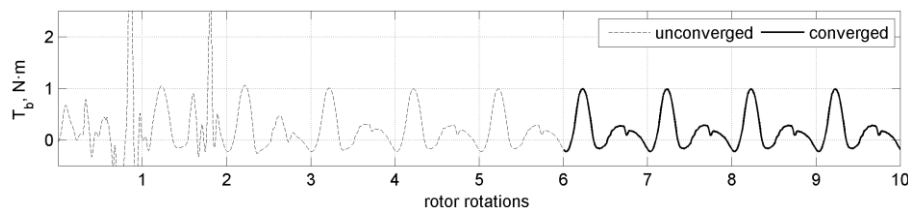
Figure 8. Blade torque ripple of one blade for 10 full rotations.

Sufficient temporal resolution is necessary to ensure proper unsteady simulation of the VAWT. Different time step sizes Δt that are equivalent to specific rotational displacements along the azimuth were tested. The largest Δt used was equal to a $\Delta t = 1°\omega^{-1}$ (time for one degree equivalent rotation) and was subsequently halved twice over to get $\Delta t = 0.5°\omega^{-1}$ and $\Delta t = 0.25°\omega^{-1}$. All three Δt's were tested at $\lambda = 2$ and $\lambda = 4$. Results for both λ are presented in Figure 9. It is clear that there is a delay in the torque ripple for the coarsest $\Delta t = 1°\omega^{-1}$ for $\lambda = 2$ while the two finer Δt's are in good agreement especially in the upwind. A small difference in predicted magnitude of T_b between $\Delta t = 0.5°\omega^{-1}$ and $0.25°\omega^{-1}$ is seen from $\theta = 280°$ to $\theta = 330°$ but the peaks

and troughs are still in sync. In terms of CP, there is negligible difference between the three Δt's with a maximum ΔCP of only 0.003. A similar agreement between the three Δt's is observed at λ = 4 with the maximum ΔCP of 0.003 as well. There is very little variation between the three cases with the only noticeable difference in the torque ripple from θ = 260° to θ = 290°. The upwind is accurately predicted by the three Δt's with all capturing the maximum T_b around θ = 80°. The maximum T_b in the downwind is also properly predicted by all Δt's at θ = 240°. Since time accurate simulations is required for this study, the chosen time step size was $\Delta t = 0.5°\omega^{-1}$ so that the vortex shedding at λ = 2 is correctly modelled and was adapted for the remaining runs.
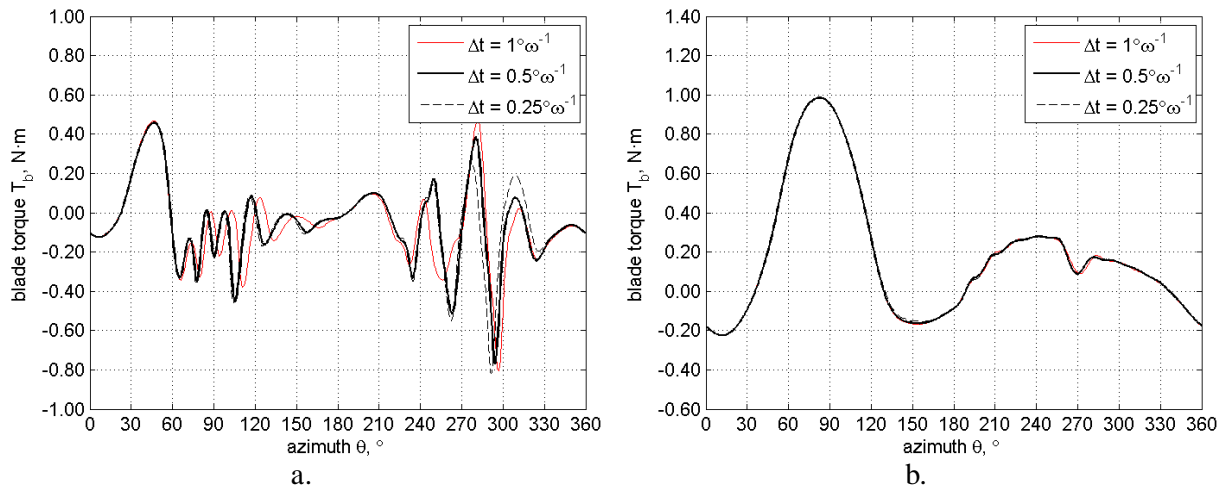
Figure 9. Time step size study results: a) λ = 2, b) λ = 4.

IV. Validation of CFD Model

The numerical model developed was checked against experimental data to assess its capability of correctly simulating VAWT flow physics. The validation is not considered exact, since the CFD model is 2D, while the actual problem is 3D. Nevertheless, a good 2D CFD model will provide substantial insight into the factors driving the performance of the VAWT and a means of checking the model's accuracy in capturing the details of the problem is presented below.

A. Power Coefficient

The first aspect of the model validation is the comparison of the predicted VAWT performance over a wide range of operating speeds. Both the fully turbulent k–ω SST and the Transition SST models were tested against the experimentally derived CP. The steady wind speed chosen was 7m/s and the simulations were run at different tip speed ratios from λ = 1.5 up to λ = 5 in increments of 0.5. It can be seen from Figure 10 that both 2D models over–predict CP starting from λ = 2 all the way up to λ = 5. Maximum CP for the fully turbulent model is 0.35 at λ = 4 while the Transition SST model predicts maximum CP = 0.33 at λ = 4.5. The maximum CP for the fully turbulent model occurs at the same λ as that of the experiments. There is a gap in the predicted CP's between the two CFD models from λ = 3 to λ = 4.5 where the fully turbulent model over–

predicts the CP much more than the Transition SST model. A convergence of the curves is seen from $\lambda = 1.5$ to $\lambda = 3$ and also from $\lambda = 4.5$ to $\lambda = 5$. Higher λ's show the greatest over–prediction of the CFD models from experiments. This may be due to the effects of finite blade span where the reduction in aspect ratio as seen by McIntosh [18] cause a substantial drop in CP at high λ versus the small drop in CP at low λ.
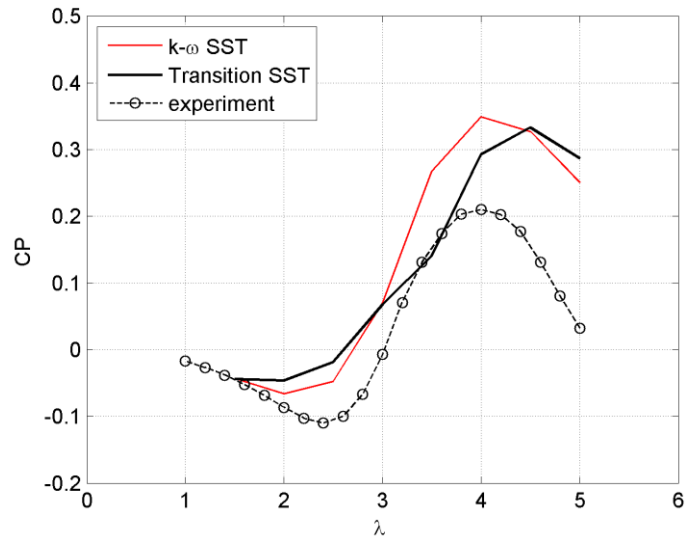
Figure 10. Steady CP curves at 7m/s.
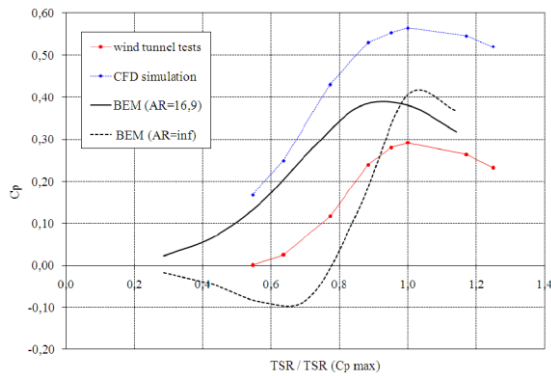
a. Raciti Castelli et al study [13].
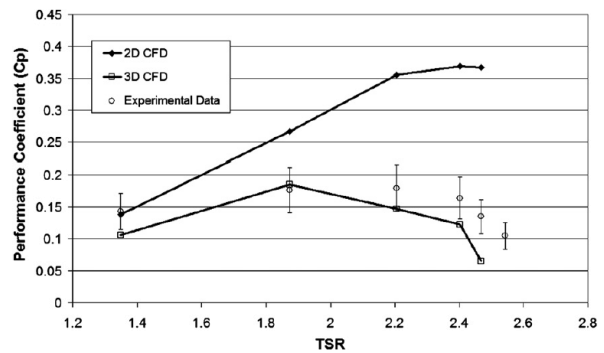
b. Howell et al study [11].
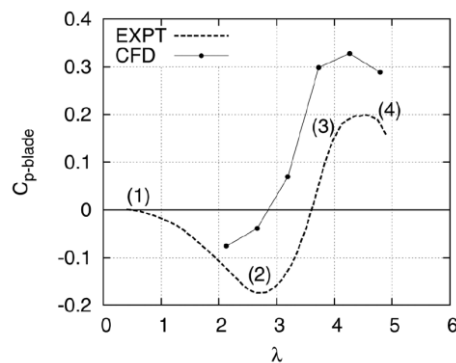
c. Edwards et al study [9].

Figure 11. Published results from other studies showing
the difference between 2D and 3D data.

The gap in predicted CP was expected since the 2D model does not account for finite blade span as well as for blade–support arm junction effects and support arm drag that are present in the actual setup. The results are consistent to published data by Raciti Castelli et al [13], Howell et al [11] and Edwards et al [9] where 2D CP is over–predicted over the entire range of λ. Raciti Castelli et al compared their 2D simulations to wind tunnel experiments (Figure 11a) and argued that the difference is due to blockage effects that increase the flow velocities near the blades to much higher values than the unperturbed flow at the inlet. Howell et al show an improved match between 3D CFD and experiments (Figure 11b). Edwards et al attribute the difference (Figure 11c) in predicted CP to finite blade span and blade–support arm junction effects.

Overall, the general trend of the predicted CP matches well with the experimental data. There is an observed negative trough at the low λ which rapidly rises and reaches maximum values near the experiment maximum at λ = 4 after which a rapid drop in CP is seen. In terms of shape, the fully turbulent model results show a smoother curve and better agreement to experiments while the Transition SST model results do not form a smooth curve and predict maximum CP at a higher λ.

B. Visualisations

The second aspect of validation is the comparison of flow visualisations between CFD and PIV. This part is an important step since the behaviour of the flow around the VAWT blades add significant insight as to why the CP varies as it does at different operating conditions. The flow physics at two λ are inspected and an assessment of the most appropriate turbulence model is performed based on the accuracy of the predicted stalling and reattachment of the flow on the blades as they go around the VAWT.

Flowfield at λ = 2

Figure 12 shows the vorticity plots for the upwind at λ = 2. At the start of the rotation, both turbulence models clearly predicts fully attached flow. There is an observed wake (green contour) seen on the lower left portion of each CFD image at θ = 10° that is also visible in the PIV image. This is the wake of the preceding blade already at θ = 130°. Flow continues to be attached until θ = 60° where both the Transition SST model and PIV reveal a bubble that is forming on the suction surface of the blade. The fully turbulent k–ω SST predicts the same formation of a separation bubble 10° later at θ = 70°. This delay has a significant effect on the blade torque since this can mean extended generation of lift that may positively affect the predicted performance of the VAWT.

As seen in the PIV at θ = 70° the separation bubble has formed into a dynamic stall vortex and has already been detached from the blade surface. This is properly captured by the Transition SST model. However, the fully turbulent model still predicts the vortex to be on the blade surface. This delay in the formation and detachment of the dynamic stall vortex affects the shedding of the subsequent pairs of leading edge and

trailing edge vortices and is evident in the presence of a trailing edge vortex in the FOV of the fully turbulent model at $\theta = 140°$ but is not seen on both the Transition SST model and PIV.

The downwind (not shown for brevity) shows better agreement between the two CFD models when it comes to the scale and timing of the shed vortices although slightly smaller when compared to the PIV. The flow reattachment is seen to have started earlier in the Transition SST model as the stall is significantly shallower at $\theta = 280°$ as compared to the fully turbulent model and PIV. This may, in part, explain the higher predicted CP at this λ. Overall, the timing and depth of stall in the upwind for the Transition SST model matches the PIV quite well while the reattachment of the flow in the downwind is better captured by the fully turbulent model.

Flowfield at $\lambda = 4$

Flow visualisations for $\lambda = 4$ are presented in Figure 13. For the most part, the flow is attached to the blade. The wake of a previous blade (green band) is visible in the lower portion of the images at $\theta = 40°$. At $\theta = 120°$, the Transition SST model shows an almost full stall on the suction surface while very light stall is seen in the fully turbulent model and PIV. Ten degrees later at $\theta = 130°$, the Transition SST model shows a deep full stall that is consistent to the PIV while partial stall is still observed in the fully turbulent model. The delay in stalling will have increased the positive performance of the fully turbulent model and pushed the CP to higher values as seen in Figure 10. At $\theta = 170°$, the fully turbulent model shows full reattachment of the flow while the PIV still shows partial separation from mid–chord to trailing edge. The Transition SST model is still stalled but to a lesser degree and produces a narrower wake when compared to PIV.

Based on the results obtained from both force and flow validation, the Transition SST model was selected as the best model that most accurately captures the flow physics of the VAWT. From the correct prediction of start of stall and the rate and scale of shed vortices at $\lambda = 2$ to the stalling and reattachment of flow at $\lambda = 4$, the Transition SST model better calculates the flow physics versus the k–ω SST model. The predicted positive performance of the Transition SST model is closer to experiemnts with lower values of CP versus the k–ω SST model. All simulations conducted for the unsteady wind study will use the Transition SST model.
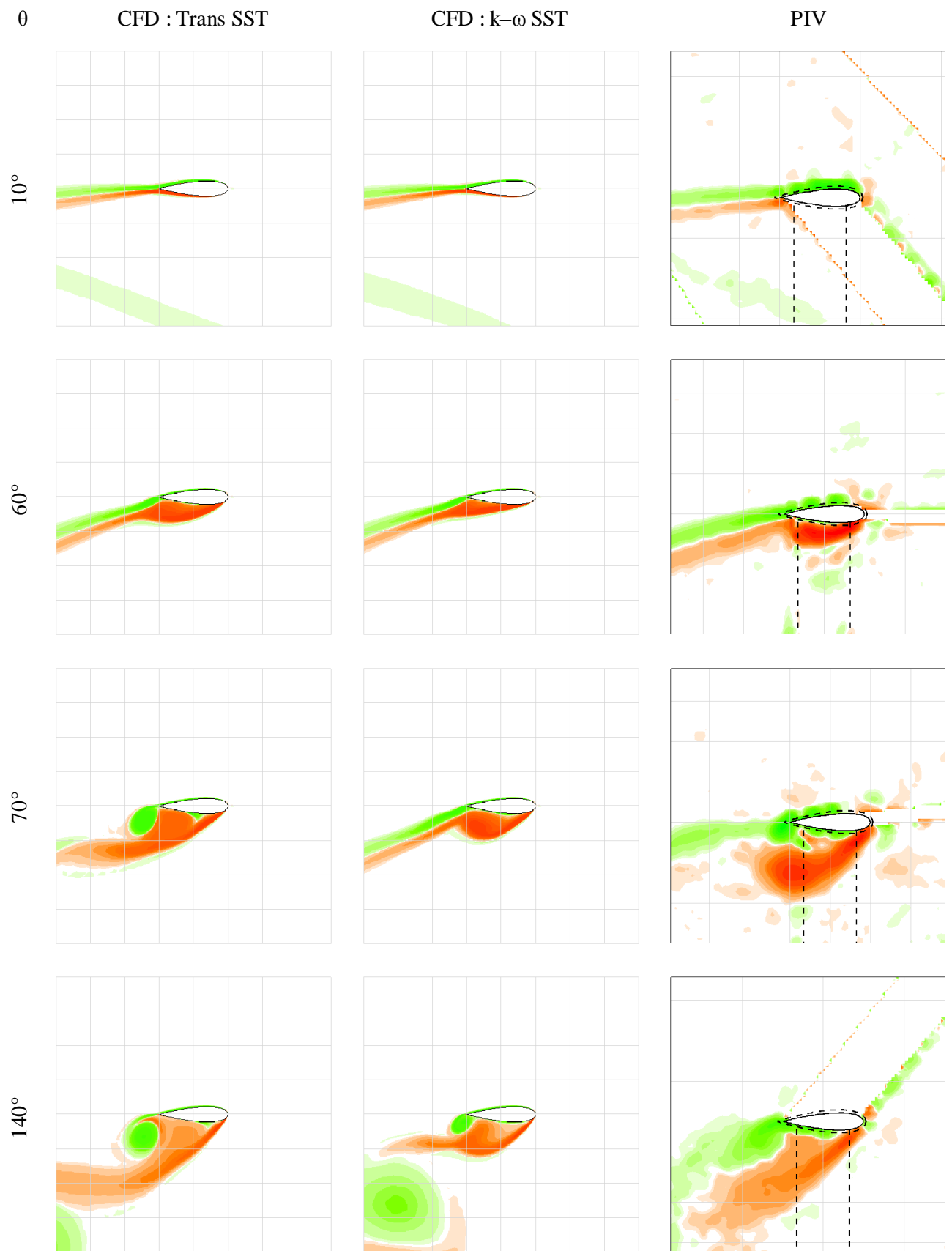
Figure 12. Flow visualisations in the upwind for λ = 2.
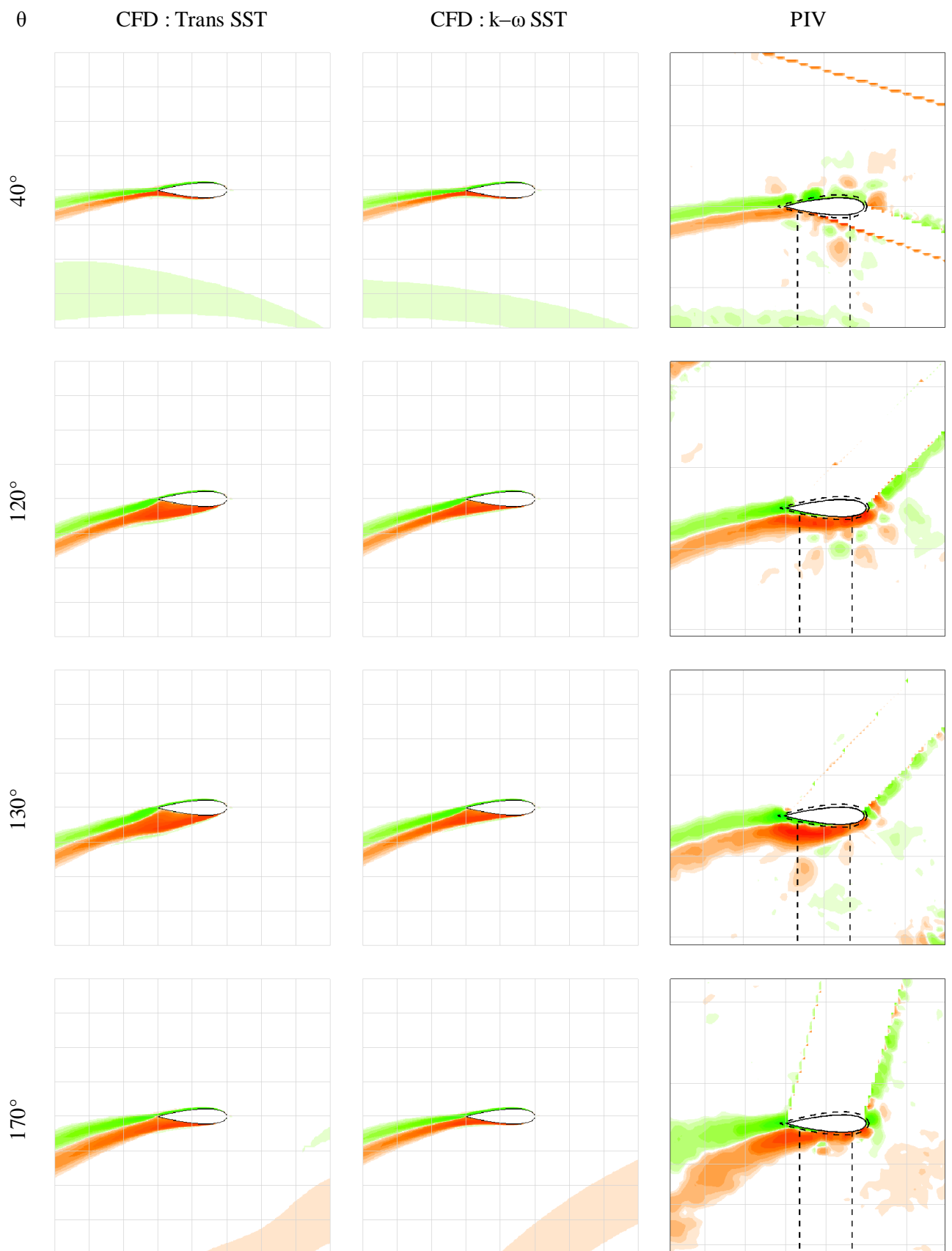
Figure 13. Flow visualisations in the downwind for $\lambda = 4$.

V. Unsteady Wind Performance

Numerical modelling of the unsteady wind inflow through the tunnel was carried out by specifying the velocity inlet magnitude as a time–dependent variable and running the simulation for approximately 1.5 wind cycles. This is necessary so as to attain not just periodic convergence in the simulations, but also to generate a contiguous set of converged data that covers the entire cycle of the wind fluctuation. It has been determined by the Author that in order to match the experimental wind cycle with a fluctuation frequency of 0.5Hz, the simulations had to be run for 40 full rotations of the VAWT. For each run, a total of about 5,400 processor hours was required to complete 40 rotations in the University of Sheffield's Intel–based Linux cluster using 16 cores of Intel Xeon X5650 2.66GHz processors.

The numerical model used in the unsteady wind simulations is the optimised model developed for the steady wind case. Apart from the varying velocity inlet boundary condition, the only other difference of the unsteady wind model is the force monitor, where not only one blade is monitored but all three. A plot of T_b for all three blades is presented in Figure 14 alongside the fluctuating free stream. The unconverged T_b is clearly shown in the first three rotations. Full convergence per time step was achieved after 6 rotations when residuals of all conserved variables fell below 1×10^{-6}. For the case shown where the VAWT rotational speed is $\omega = 88$rad/s, one wind cycle is about 28 VAWT cycles.
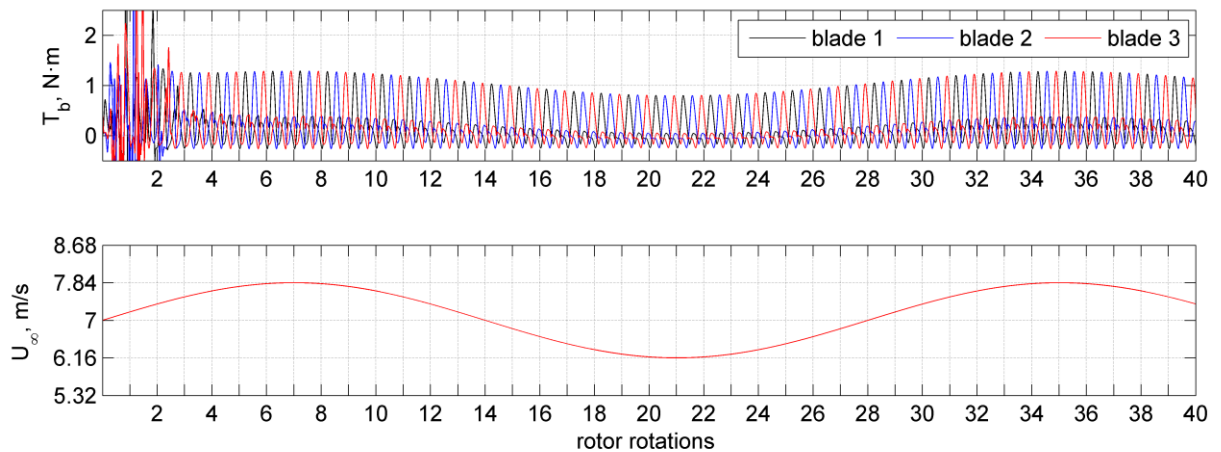
Figure 14. Plot of unsteady T_b and U_∞ over 40 VAWT rotations.

One major assumption in the computation of unsteady CP is the free stream velocity in the wind power term. Since the inlet velocity is the specified parameter in all simulations, one may assume that there is a delay in the fluctuating wind that the VAWT sees as a consequence of its position downstream. However, the model is constrained within the wind tunnel and conditions are well within the limits of incompressible flow regime. As such, a change in the inlet velocity results in the entire domain changing in flow velocity. A test was conducted to verify this assumption by running a simulation with an empty wind tunnel domain under fluctuating velocity inlet condition. Seven monitor points were placed between the two wall boundaries along the length of the domain. Results confirm the incompressible assumption and are shown in Figure 15.
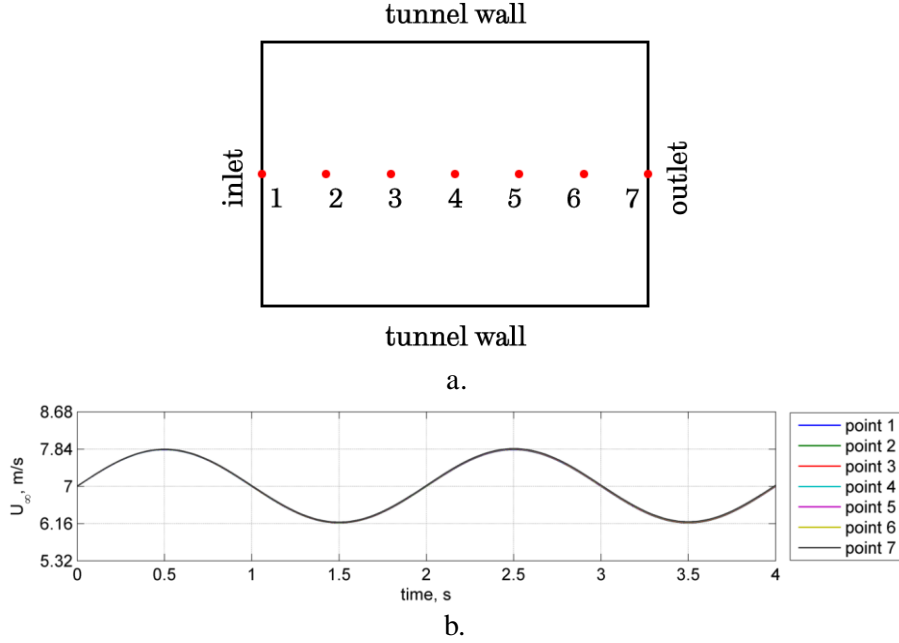
Figure 15. Study of U_∞ variation in an empty tunnel domain with fluctuating inlet condition: a) position of monitor points along tunnel length, b) results of simulation supporting incompressibility assumption.

A. Reference Case

A reference case is selected to act as the baseline model to which parametric variations are compared. The mean wind speed is U_{mean} = 7m/s with a 12% fluctuating amplitude of U_{amp} = ±12% (±0.84m/s) and fluctuation frequency of f_c = 0.5Hz. The rotor angular speed is a constant ω = 88rad/s (840rpm) resulting in a mean tip speed ratio of λ_{mean} = 4.4. When inspected against the steady CP curve, this condition is just before peak performance at λ^* = 4.5. Although this λ_{mean} is greater than the highest experimental λ_{mean} of 4.1 (see Sec. 5.3.1), its position in the steady CP curve matches closely to the low λ_{mean} case of the experiments that was just below peak performance.

A total of 28 rotor rotations completes one wind cycle. As shown in Figure 16, the λ changes with the fluctuating U_∞. Increasing U_∞ causes the λ to fall owing to their inverse relationship and a constant ω. Maximum U_∞ is 7.84m/s and occurs at the end of the 7th rotation with λ dropping to its minimum of 3.93. The maximum α of each blade per rotation can be seen to increase with the increasing U_∞ reaching a peak value of α = 14.74° between the 6th and 8th rotation depending on the blade considered. Following the maximum U_∞ is the gradual drop of U_∞ back to the mean wind speed. It continues to fall until it reaches the minimum value of U_∞ = 6.16m/s at the end of the 21st rotation. At this U_∞, the λ rises to its maximum value at 5.0. Within this part of the wind cycle, the maximum α per rotation falls to 11.55° between the 20th and 22nd rotation depending on the blade in question. The subsequent increase of U_∞ back to the mean value causes the λ to drop in magnitude and the peak α per rotation to increase.
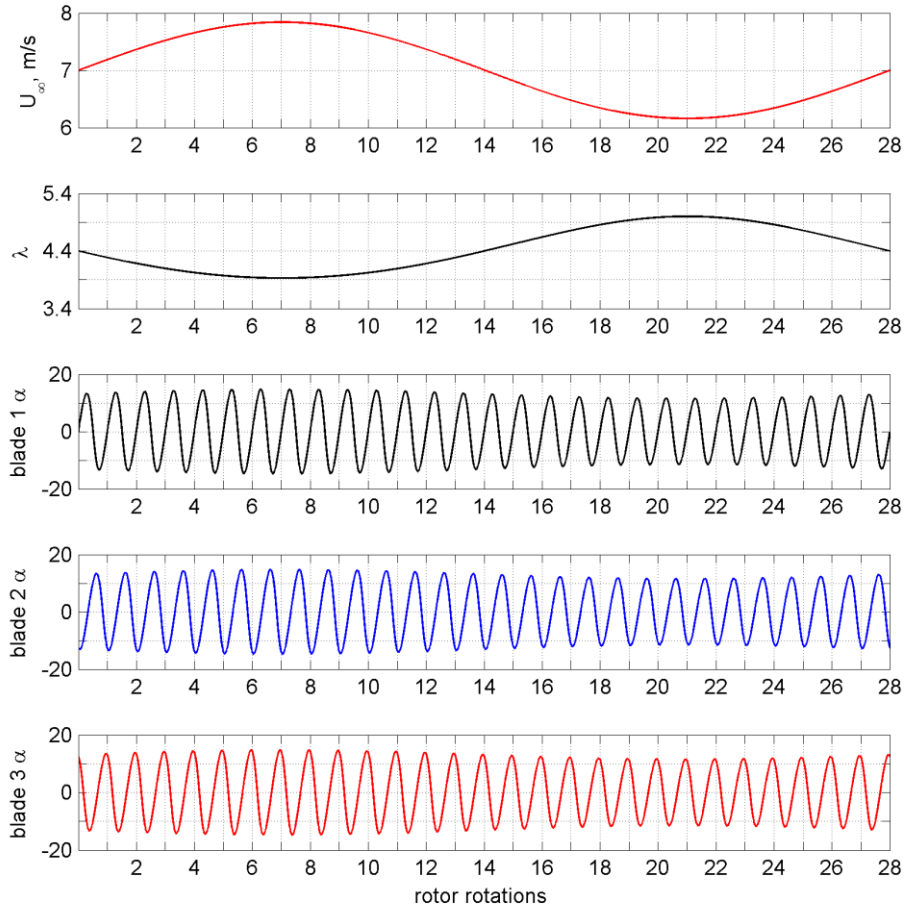
Figure 16. Variation of U_∞, λ, and α for the reference case.

The peak T_b of each rotor cycle increases together with increasing U_∞, all three blades showing similar trends and each with maximum T_b value of roughly 1.28N·m generated within the 8th rotation (Figure 17). The maximum combined blade torque T_B is 1.59N·m, also within the 8th rotation. In the second half of the wind cycle, the peak T_b of each rotor cycle drops to 0.79N·m within the 22nd rotation for each of the three blades while the lowest peak T_B registers at 0.76N·m within the same rotor cycle. It is observed that T_B is mostly positive, which suggests positive overall performance. Also, the huge fluctuations in the T_B with characteristic frequency equal to three times the rotor frequency would result in huge fluctuations in the rotor power P_B. The variation of P_B is shown in Figure 18 together with the fluctuating wind power P_w. As expected, the peaks of P_B follow the wind variation much like the T_B does. Maximum P_B is 140Watts generated as P_w maximizes at the end of the 7th rotation, with magnitude of 207W. Also presented are the unsteady CP and quasi–steady CP using moving average smoothing. Smoothing the unsteady CP provides a useful comparative plot to the experimental data presented in the Chapter 5, where the unsteadiness of the experimental CP over one rotor cycle is not captured. In addition, this is shown to be consistent with the cycle averaged method of computing for the rotor CP in steady wind conditions, that filters out the fluctuating nature of the blade torque to give a single value prediction of VAWT performance.
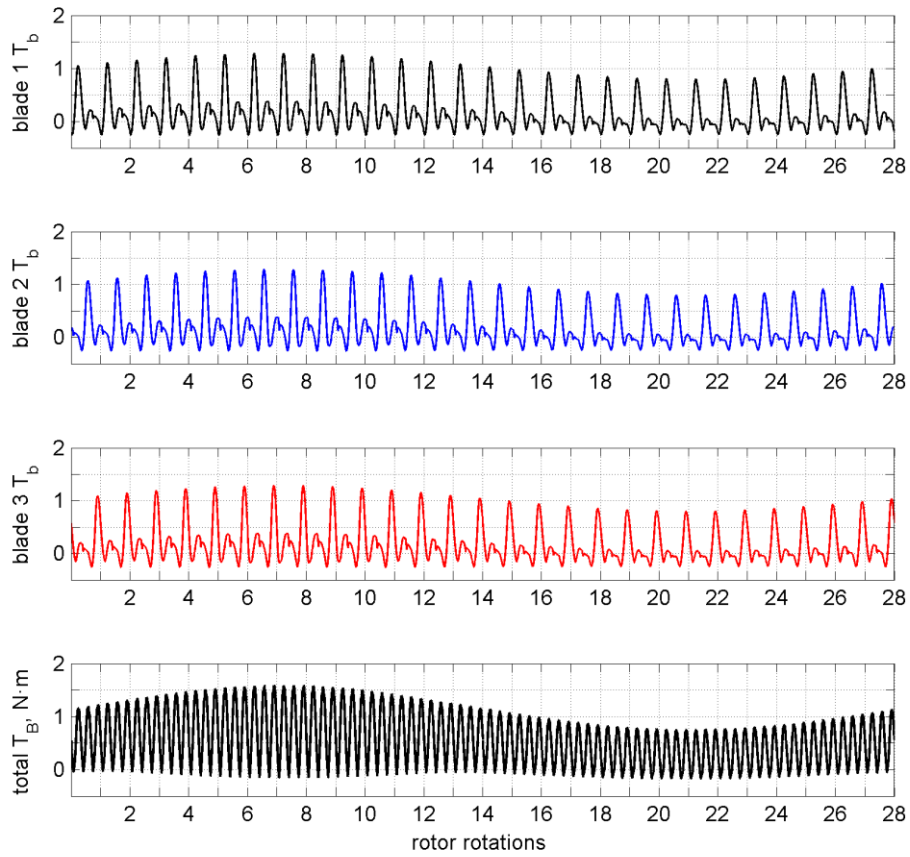
Figure 17. Variation of T_b and T_B for the reference case.
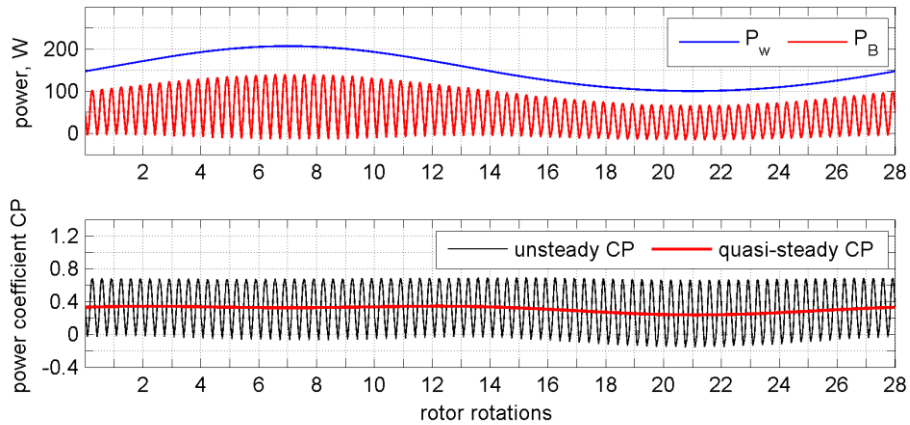
Figure 18. Variation of power and CP through one wind cycle.

In Figure 19, the plots of the unsteady CP and quasi–steady CP versus λ are shown relative to the steady wind performance at 7m/s. The fluctuations in the unsteady CP over the band of operating λ show a massively varying VAWT performance that greatly exceeds the limits of the steady wind CP. The maximum CP is recorded at 0.69 and occurs just after the 15th rotation ($\lambda = 4.55$). The minimum CP is seen to take place after the 21st rotation with a value of -0.15 ($\lambda = 5$). The wind cycle–averaged CP is computed to be 0.33 ($\lambda_{mean} = 4.4$) and is equal to the maximum steady wind CP of 0.33 at $\lambda = 4.5$. It is clear from the figure that the quasi–steady CP crosses the steady CP curve in a similar manner as presented in the experimental results in Sec. 5.3. Increasing wind speeds cause the CP to deviate from the steady CP curve and rise to higher levels as the λ

falls to lower values. On the other hand, decreasing wind speeds cause the CP to drop below the steady CP curve as the λ rises. This behaviour is consistent to the Reynolds dependent nature of the quasi–steady CP discussed in Sec. 5.3. There is no discernible hysteresis in the quasi–steady CP curve.
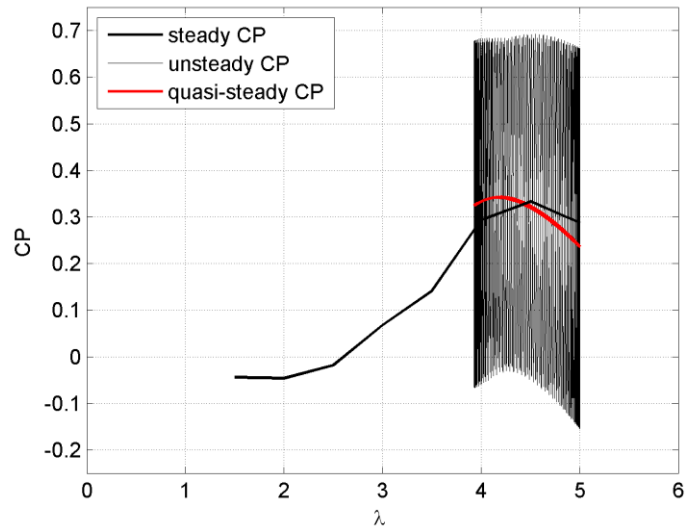
Figure 19. Performance of the VAWT in 12% fluctuating free stream.

a.   b.
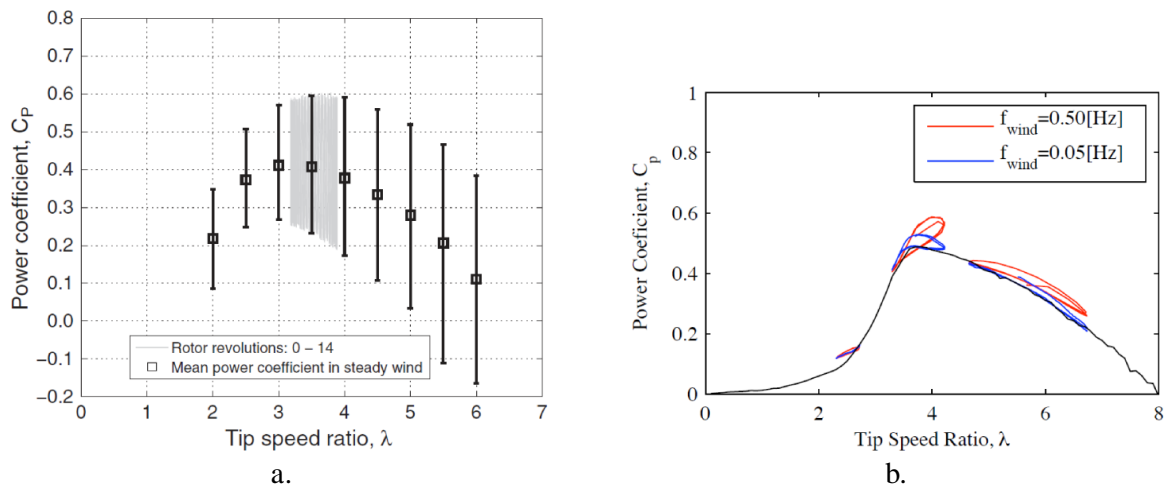
Figure 20. Unsteady wind results of two numerical studies:
a) Scheurich and Brown [19], b) McIntosh et al [20].

Scheurich and Brown [19] observed similar results in the unsteady CP from their vortex transport model. At a low frequency of wind fluctuation $f_c = 0.1$Hz, a 5kW scale VAWT with a radius of $R = 2$m takes 14 full rotations to complete one wind cycle. The unsteady CP varies greatly in magnitude even for fluctuations in wind speed of only 10%. As shown in Figure 20a, the unsteady CP fluctuates within the limits of the steady wind CP variations. They theorize that the VAWT with swept blades essentially traces the steady CP performance curve when subjected to unsteady wind with low f_c's. A similar conclusion is derived by McIntosh et al [20] in their free vortex model. They do not present a highly fluctuating unsteady CP but a quasi–steady CP based on an assumption that the VAWT CP is a function solely of λ evaluated at the centre of the rotor. This assumption requires steady CP curves of different wind speeds as the basis for the lookup of unsteady wind CP thereby eliminating the aerodynamic fluctuations as seen by the blades. Their results show

that at low $f_c = 0.05$Hz, the quasi–steady CP traces the steady CP curve at λ higher than λ^* (Figure 20). It can be deduced from the results of both studies that a fluctuating free stream is not detrimental to the VAWT performance. There is a chance of increased performance as predicted by McIntosh in conditions near peak steady CP while Scheurich asserts a VAWT unsteady CP can be traced using steady CP curves.

The lift coefficient loops for selected cycles are shown in Figure 21. It is evident that all cycles exceed the static stall lift in the upwind (Figure 21b) with maximum $C_l = 0.94$ generated during the 7th rotor cycle. At this point in the wind cycle, the wind speed is nearing its maximum value. Lowest peak of C_l loop is seen at the 22nd rotor cycle when the wind speed is close to its minimum. Downwind performance is not so similar. Maximum C_l of 0.71 is still generated in the 7th rotor cycle (Figure 21c). However, all rotor cycles within the second half of the wind cycle (cycles 15th to 28th) see their C_l not exceed the static stall lift.
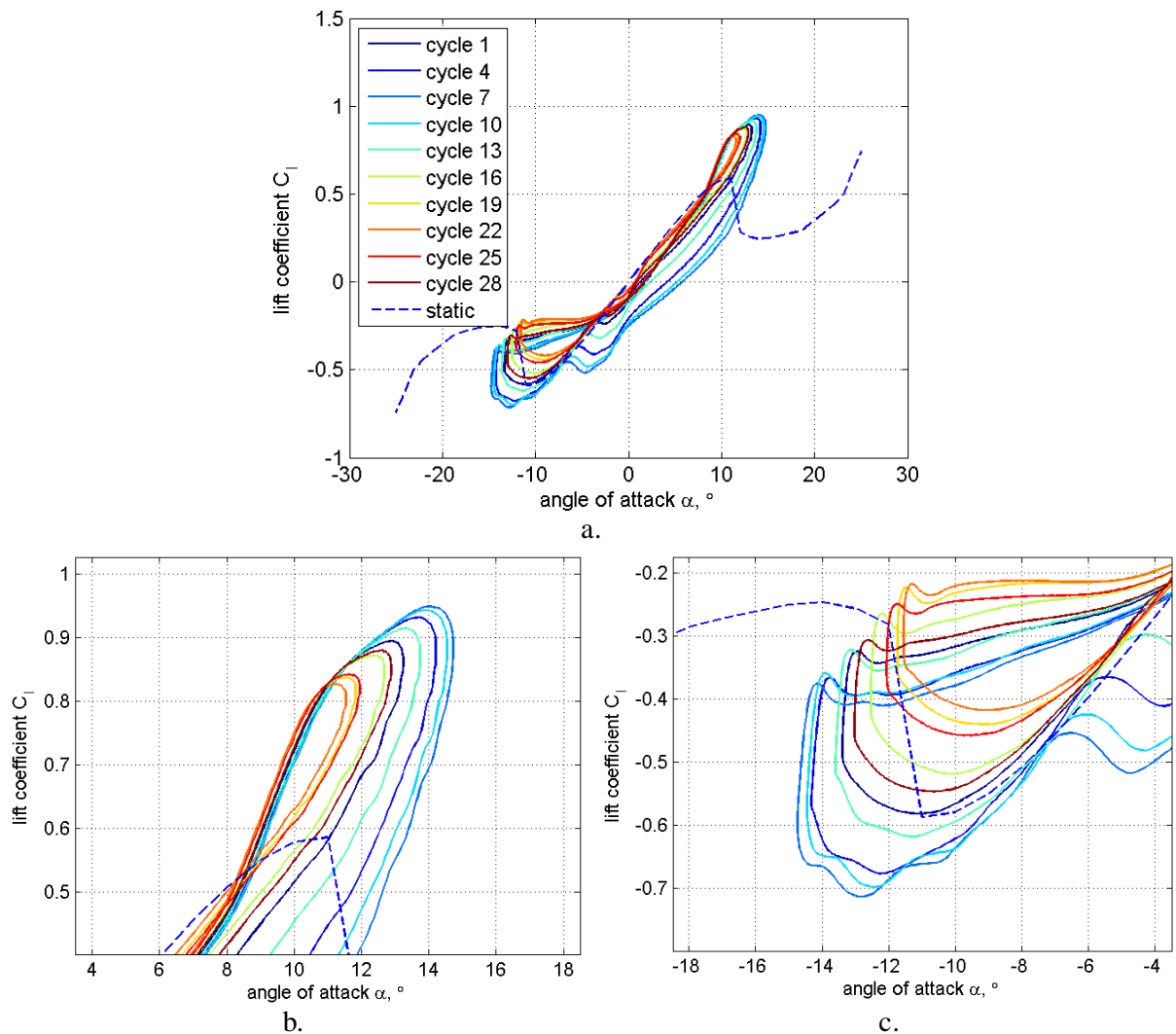
Figure 21. Lift coefficient plot for the reference case: a) full plot of cycles,
b) zoom view of upwind loops, c) zoom view of downwind loops.

The drag coefficient loops for selected cycles are shown in Figure 22. It can be seen that all cycles exceed the static stall drag in the upwind (Figure 22b) with maximum $C_d = 0.14$ generated during the 7th rotor cycle. The trends of the C_d loops seem to follow the C_d line of the stalled condition for static aerofoil indicating that not only increases in lift are observed, but also in drag. Downwind drag does not follow the same trend. Maximum C_d of 0.09 is still generated in the 7th rotor cycle (Figure 22c). However, all rotor cycles have their C_d loops follow the C_d line of the un–stalled condition for a static aerofoil.

Although maximum C_l is at the 7th cycle, this is counteracted by the C_d, which is also at its maximum. Hence, the quasi–steady CP is not at its peak when U_∞ is at the highest value. In fact, maximum quasi–steady CP is seen to occur at the 3rd and 12th cycles, when maximum C_d is 15% lower than the 7th cycle maximum of 0.14 while maximum C_l is only 2% lower than the 7th cycle maximum of 0.94.
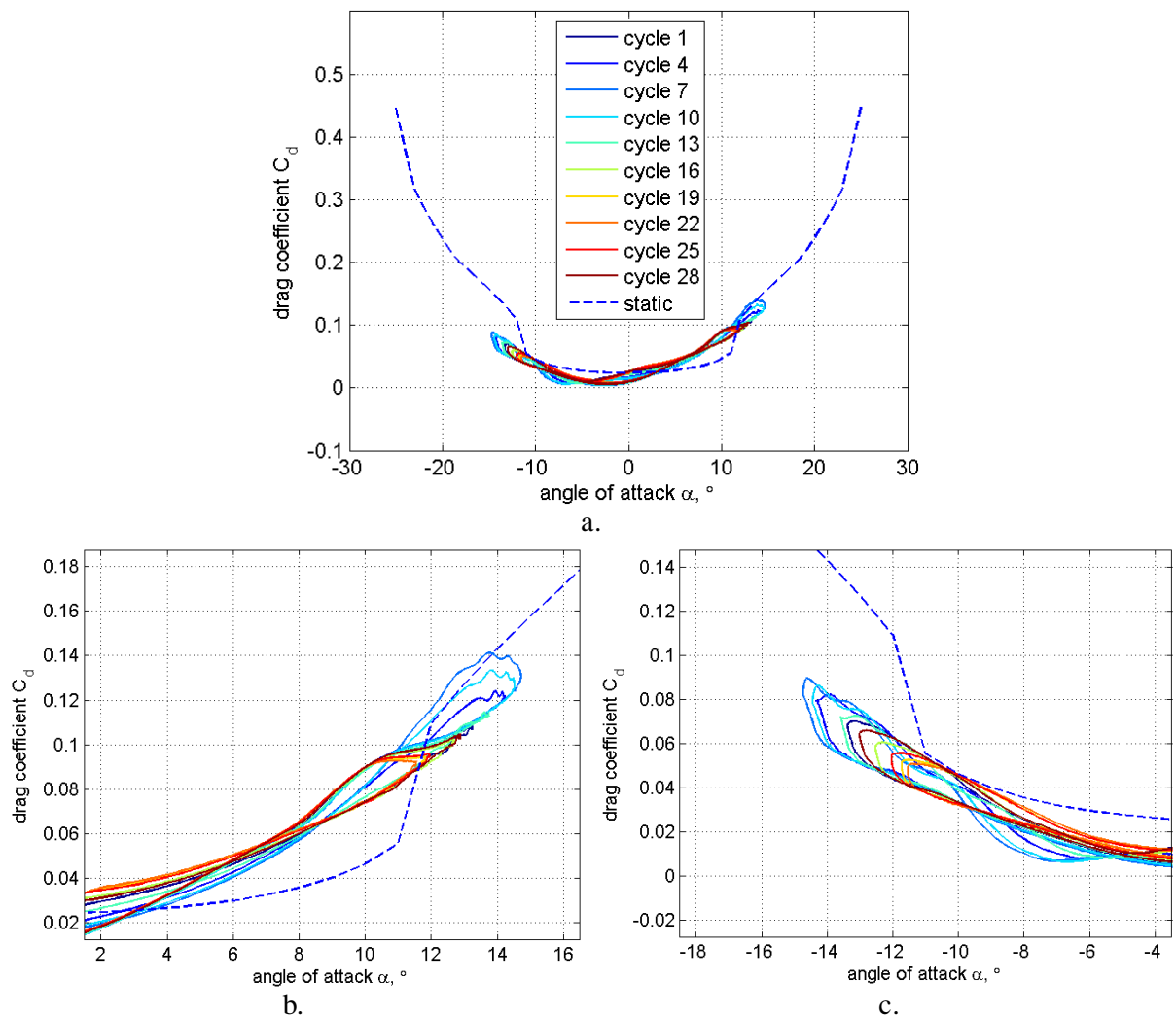
Figure 22. Drag coefficient plot for the reference case: a) full plot of cycles, b) zoom view of upwind loops, c) zoom view of downwind loops.

Flowfield visualisations of the reference case are shown in Figure 23. Only selected cycles and azimuth positions are shown for brevity, since a complete set of visualisations for an entire wind cycle will compose of 3,024 images from three blades that see completely different free stream conditions at a conservative 36 azimuth positions per rotor cycle. The first half of the wind cycle has been selected since most of the interesting flow features occur at λ lower than λ_{mean}, whereas higher λ would only show mostly attached flow with light or no separation at all. Presented are visualisations using vorticity at azimuth positions with the deepest stall for each blade in the upwind region of the rotor cycle shown.

blade 1   blade 2   blade 3
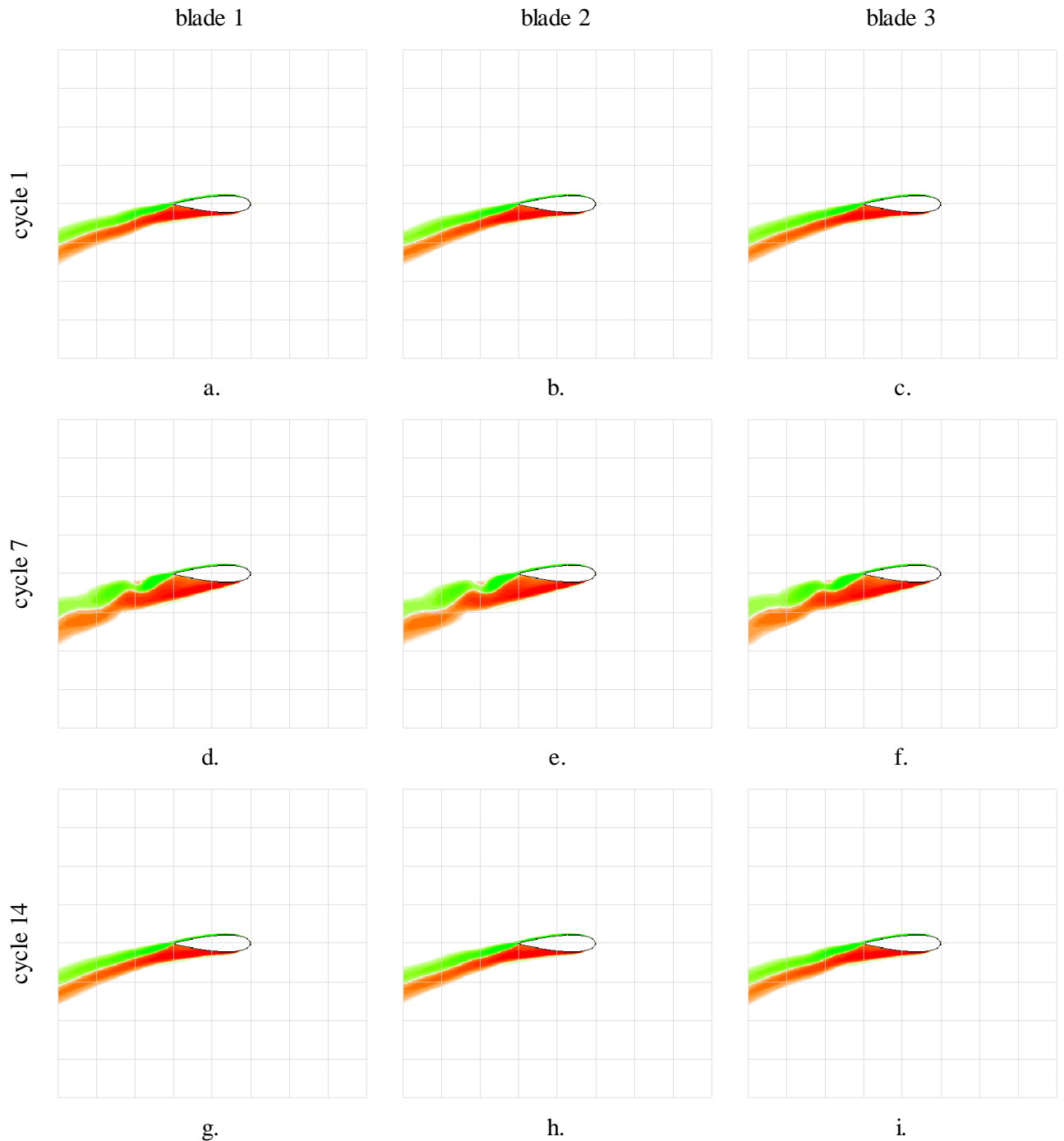
Figure 23. Flow visualisations of vorticity from selected rotor cycles in the first half of the wind cycle of the reference case: a to c − θ = 130°; d to f − θ = 140°; g to i − θ = 130°.

It is clear that as the wind speed increases, the stall on blade 1 becomes deeper and occurs at a later azimuth (Figure 23a & d) due to decreasing λ. Also, the separation point moves from mid–chord to the leading edge. As the wind speed falls back to U_{mean}, λ increases, the depth of stall reduces, deepest stall occurs at an earlier azimuth, and the separation point moves back to mid–chord position (Figure 23d & g). A similar observation is seen for blades 2 (Figure 23b, e & h) and 3 (Figure 23c, f & i). One thing to point out is there is no visible difference between the three blades at the same θ. The reason behind this is the low frequency of the wind speed cycle compared to the rotor cycle causing a quasi–steady condition relative to the VAWT. As blades pass a specific θ within one rotation, the free stream wind speeds between blades differ by only 0.04m/s. Furthermore, the stalling mechanism at cycle 14, where the wind speed has dropped back to U_{mean} is very similar to the stalling in cycle 1. For the full +12% change in the wind speed, the azimuth of the deepest stall in the upwind region changes by only 10° from 130° in cycle 1 to 140° in cycle 7 and goes back again to 130° in cycle 14.
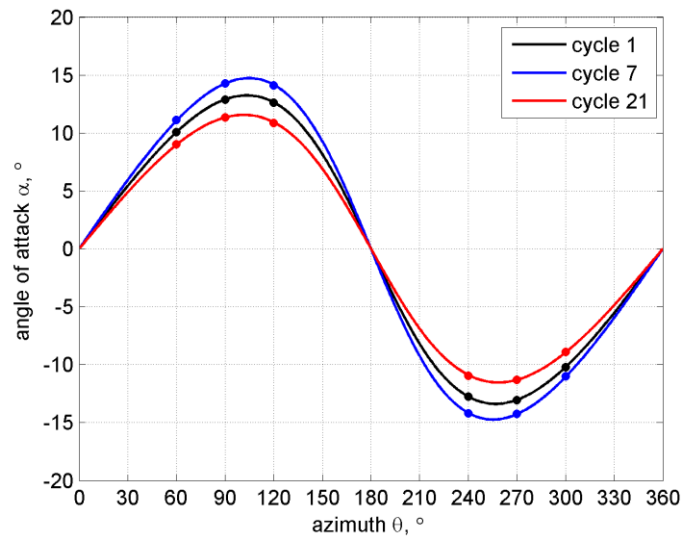
Figure 24. Variation of angle of attack for the three chosen rotor cycles.

A second set of rotor cycles has been chosen to illustrate the effects of extreme conditions within the wind cycle that a blade is subjected to and the resulting blade forces generated under such conditions. The variation of α for the three cycles, namely 1, 7, and 21, is shown in Figure 24 for reference. In this section of the analysis, attention is directed to only one blade, due to the quasi–steady condition previously seen between the three blades within one rotor cycle.

The first condition analysed is cycle 1, where the conditions are close to the mean wind speed of $U_{mean} = $ 7m/s. At this condition, the blade does not experience deep stall and no large vortices are shed at any point in the cycle. Partial separation is observed in the upwind region (Figure 25a–c) with the deepest stall occurring at $\theta = 130°$ (not shown). At $\theta = 0°$ corresponding to $\alpha = 0°$, the computed C_l is negative at –0.1 (Figure 25d). At this azimuth, the blade velocity vector is parallel to the free stream wind vector hence $\alpha = 0°$. However, the local streamlines within the blade vicinity are actually diverted due to the impedance of the VAWT, causing streamtube expansion and resulting in a local effective α that is negative. From $\theta = 0°$ up to $\theta = 60°$, C_l (Figure

25d) is seen to steadily rise along with the increase in C_d (Figure 25e). C_l at $\theta = 60°$ is already greater than the static stall lift indicating dynamic stall has been initiated.

a. $\theta = 60°$

b. $\theta = 90°$

c. $\theta = 120°$

d. C_l vs. α

e. C_d vs. α

f. $\theta = 240°$

g. $\theta = 270°$

h. $\theta = 300°$

i. T_b vs. θ
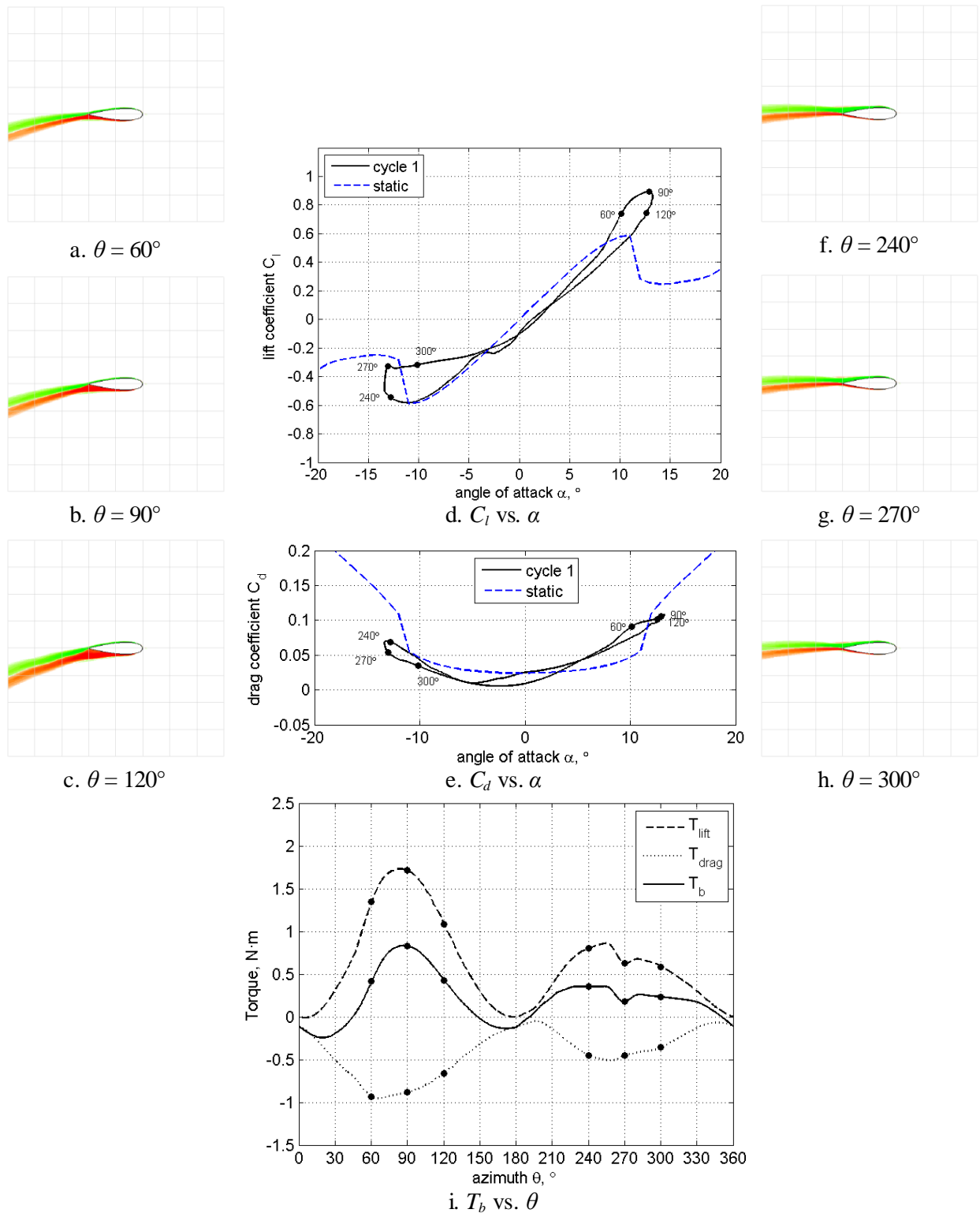
Figure 25. Visualisations and blade forces generated within cycle 1 of the reference case.

As shown in Figure 25a, there is no visible flow separation on the blade. With further rotation of the blade to $\theta = 90°$ C_l reaches maximum at 0.89 with the traling edge region starting to show separation creeping towards mid–chord (Figure 25b). The C_d slightly rises from 0.09 at $\theta = 60°$ to $C_d = 0.11$ at $\theta = 90°$ but its tangential component T_{drag} is lower (Figure 25i), because of a higher perceived α from 10.1° at $\theta = 60°$ to 12.9° at $\theta = 90°$. As the blade passes $\theta = 120°$, C_l has dropped to 0.75, while C_d is still high at 0.10. At this point in the rotation, the blade already shows mid–chord to trailing edge separation, which is the primary cause of the high drag. The low lift, the high drag and a slightly lower α of 12.6° versus the $\theta = 90°$ position (Figure 24) means that T_b at $\theta = 120°$ is predicted to be significantly lower at 0.43N·m, 48% lower than the T_b at $\theta = 90°$ which is calculated to be 0.83N·m. T_b crosses the zero line into the negative region at $\theta = 147°$. A hysteresis loop is seen in the C_l due to the more rapid 'pitch down' motion of the blade in the second quadrant.

The entire downwind region showed attached flow, with C_l values below static stall prediction. Although the computed α at $\theta = 240°$ is $-12.8°$, the T_b is seen to be 0.36N·m. This is lower than the predicted T_b at $\theta = 120°$ mainly because the flow velocity has already dropped in the upwind region resulting in a higher relative flow velocity, a likely lower effective α than the geometric $-12.8°$, the drag being more aligned to the tangential direction than lift, and hence lower T_b. C_l reduces from 0.54 at $\theta = 240°$ to 0.33 at $\theta = 270°$ clearly due to the centre shaft wake that reduces the flow velocity in this portion of the blade path. A more pronounced hysteresis loop of the C_l is observed in the downwind most likely due to combined effects of the skewed sinusoid variation of α and the reduced, assymmetric flow velocity. C_l at $\theta = 300°$ is 0.32, C_d is 0.03, while T_b is 0.23N·m and gradually get smaller until it drops to the negative region as the blade passes $\theta = 350°$.

The second condition analysed is the first extreme condition that the VAWT sees at the 7th rotor cycle where U_∞ approaches its maximum value of 7.84m/s. At this point in the wind cycle, the λ is pushed from 4.4 down to 3.93. With the reduction in λ come increased α (maximum value at 14.73° versus 13.24° for cycle 1, Figure 24) and subsequently higher C_l and C_d. From a value of 0.89 in cycle 1, C_l rises to 0.95 at the same azimuth position of $\theta = 90°$ (Figure 26d). A significant drop in C_l to 0.71 is observed at $\theta = 120°$ creating a much larger hysteresis in the C_l loop. In fact, C_l forms a hysteresis loop throughout the entire cycle. Much higher perceived α means a steeper and faster 'pitch down' motion in the second quadrant inducing stalled flow that is worse than what is seen in cycle 1. Stall is developed on the blade surface as shown in Figure 26c that is much deeper when compared to the same azimuth in cycle 1 (Figure 25c). Deepest stall is at a later azimuth of $\theta = 140°$ (not shown) accompanied by a rippled and much thicker wake. Maximum torque due to lift (T_{lift}) in the upwind jumps to 2.07N·m for cycle 7 from 1.73N·m for cycle 1. However, the drag contribution to torque (T_{drag}) barely changes from a maximum of -0.95N·m for cycle 1 to -1.04N·m for cycle 7. This explains the difference in maximum T_b in the upwind between the two cycles where $T_b = 0.83$N·m for cycle 1 and $T_b = 1.04$N·m for cycle 7.

Downwind performance follows the same trend with higher T_b observed in cycle 7 dictated mostly by the higher C_l and comparable C_d generated by the blade. C_l at $\theta = 240°$ rises from 0.54 in cycle 1 to 0.66 in cycle 7, while C_d barely changes from 0.07 in cycle 1 to 0.08 in cycle 7 resulting in higher T_b for cycle 7. No visible flow separation is seen except for $\theta = 200°$ (not shown) when the blade interacts with a high vorticity wake of a previous blade pass inducing a mid–chord to trailing edge partial stall.

a. $\theta = 60°$

b. $\theta = 90°$

c. $\theta = 120°$

d. C_l vs. α

e. C_d vs. α

f. $\theta = 240°$

g. $\theta = 270°$

h. $\theta = 300°$

i. T_b vs. θ
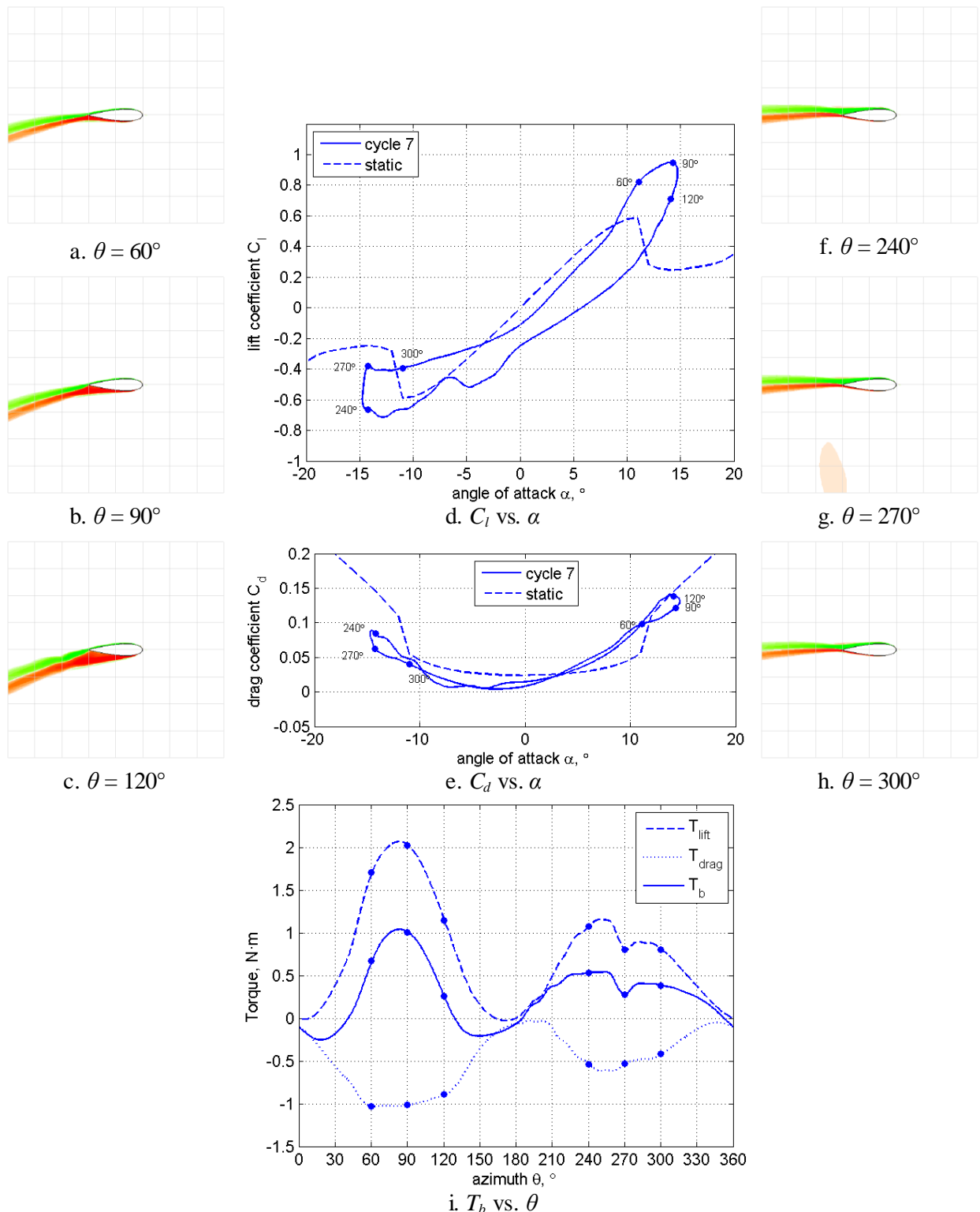
Figure 26. Visualisations and blade forces generated within cycle 7 of the reference case.

a. $\theta = 60°$

b. $\theta = 90°$

c. $\theta = 120°$

d. C_l vs. α

e. C_d vs. α

i. T_b vs. θ

f. $\theta = 240°$

g. $\theta = 270°$

h. $\theta = 300°$
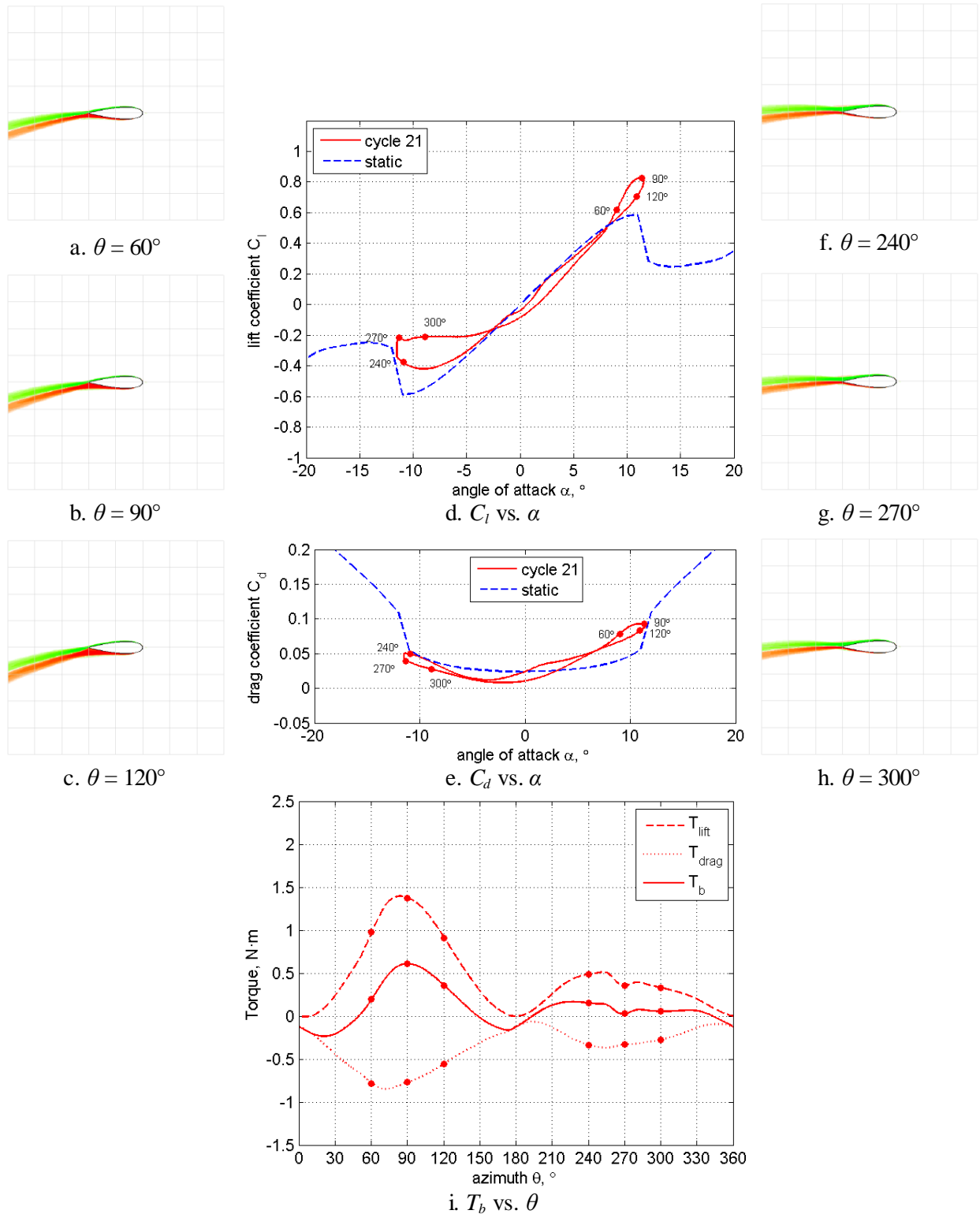
Figure 27. Visualisations and blade forces generated within cycle 21 of the reference case.

The third condition analysed is the other extreme condition that the VAWT is subjected to within the wind cycle. At the 21st rotor cycle, U_∞ has dropped to its minimum value of 6.16m/s, thereby increasing the λ to its highest value of 5. As a result, the α as seen by the blades reduces with a maximum value just slightly exceeding static stall angle at 11.56° (Figure 24). Maximum C_l recorded still exceeds static stall value of 0.83 at $\theta = 90°$ (Figure 27d) but is 7% lower than the maximum C_l of cycle 1 and 13% lower than the maximum at cycle 7. This is expected because limiting the α perceived by the blades also limits the maximum lift that the

blades generate. A milder 'pitch down' motion minimises the hysteresis of the C_l loop and suppresses the enlargement of trailing edge separation in the upwind (Figure 27a–c), essentially throughout the entire rotor cycle. A mild separation of flow is observed from $\theta = 120°$ to $\theta = 140°$ (not shown) with the separation point only a quarter chord from the trailing edge at worst.

Downwind C_l values do not reach static stall lift with the maximum value only at 0.42 (Figure 27d), 22% reduction in the maximum downwind C_l of cycle 1. T_{lift} at $\theta = 240°$ is 0.49N·m while T_{drag} is −0.34N·m resulting in a low T_b of 0.15N·m, less than half of the T_b in cycle 1 at the same azimuth and less than a third that of cycle 7 at the same azimuth. The fourth quadrant performance is very poor with maximum T_b registering at only 0.08N·m.

B. Effect of Varying the Mean λ

The reference case ω was a constant 840rpm giving a $\lambda_{mean} = 4.4$. To investigate the effects of different λ_{mean}, two simulations were run at $\omega = 78$rad/s (745rpm) and $\omega = 95$rad/s (907rpm) resulting in $\lambda_{mean} = 3.9$ and $\lambda_{mean} = 4.75$, respectively. The variation of λ in time for the three λ_{mean} cases is shown in Figure 28a. Looking at the reference case of $\lambda_{mean} = 4.4$, the maximum λ is recorded at 5.0, while the minimum is at 3.93. The peak–to–peak value is for this case is 1.07. The case with the highest λ_{mean} at 4.75 shows the maximum λ has moved up to 5.4, while the minimum is now at 4.24 resulting in a peak–to–peak value of 1.16. The opposite behaviour is observed when λ_{mean} is lower at 3.9. The maximum λ is seen to be 4.43 while the minimum is 3.48, giving a peak–to–peak value of 0.95. With the same fluctuation amplitude of $U_{amp} = \pm 12\%$, the peak–to–peak value increases as the λ_{mean} increases; an expected consequence of the direct relationship of ω and λ. The trends of the CP curves do not follow the simple and straightforward trend of λ. It can be seen in Figure 28b that the behaviour of CP as U fluctuates depends on the λ at the start of the cycle. The reference case, which starts at $\lambda = 4.4$, is closest to the steady CP maximum λ^* of 4.5. As a result, the starting CP = 0.33 is highest of the three cases. The $\lambda_{mean} = 4.75$ case comes next with a starting CP of 0.31 and the $\lambda_{mean} = 3.9$ case is last with a starting CP of 0.27. Both $\lambda_{mean} = 4.4$ and 4.75 cases see their CP rise as the wind speed increases while the $\lambda_{mean} = 3.9$ case CP falls with increasing wind speed. The position of the starting λ of the $\lambda_{mean} = 3.9$ case is way lower than λ^* and is within the drop–off part of the steady CP curve. Low λ's mean higher α and greater occurrence of stalled flow that lead to poorer performance. Maximum CP for the $\lambda_{mean} = 4.75$ case is 0.37 and coincides with the point of maximum wind speed and minimum λ. The other two cases do not have their maximum CP at the extreme values of U_∞ but rather between the U_{mean} and a U_∞ extremum. Minimum CP for the $\lambda_{mean} = 3.9$ case is 0.2 and occurs at the point of maximum wind speed and minimum λ while the other two cases have their minimum CP at the point of minimum wind speed and maximum λ.

λ_{mean}	3.9	4.4	4.75
cycle–averaged CP	0.24	0.33	0.35

Table 1. Wind cycle–averaged CP at different λ_{mean}.
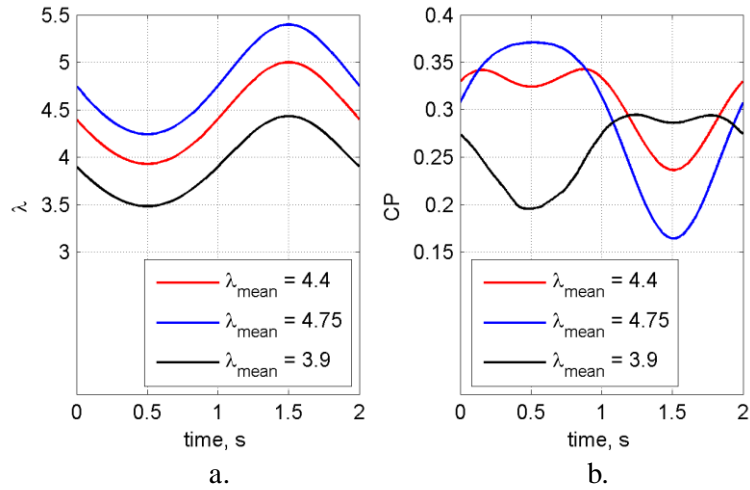
Figure 28. Quasi–steady performance of the VAWT for the different λ_{mean} cases:
a) λ vs. time, b) CP vs. time.

As can be seen from Figure 29, all quasi–steady CP curves cross the steady CP curve as the wind fluctuates. For the λ_{mean} = 4.75 case, maximum CP is 0.37 at λ = 4.24 while minimum CP is 0.16 at λ = 5.4. These two points are essentially the points of maximum and minimum wind speeds in the wind cycle. At this λ_{mean}, an increase in wind speed induces an improvement in the performance of the VAWT while falling wind speeds cause the VAWT performance to drop. The cycle–averaged CP, defined as the ratio of the mean blade power P_B to the mean wind power P_w over one wind cycle, is 0.35 which is higher than the maximum steady wind CP of 0.33 at λ = 4.5 and also higher than the cycle–averaged CP of the reference case equal to 0.33. The case when λ_{mean} = 3.9 shows a contrasting behaviour. As the wind speed increases, the quasi–steady CP falls together with the decreasing λ. At the minimum λ = 3.48, the CP is at its lowest with a value of 0.2. Maximum CP is attained in the second half of the wind cycle with a value of 0.29 at λ = 4.24. At maximum λ = 4.43 when the wind speed is at its lowest, the computed CP is 0.28. The cycle–averaged CP for this case is 0.24. An interesting result of all three cases is the λ^* of maximum CP. All cases have their maximum CP close to λ^* = 4.2.
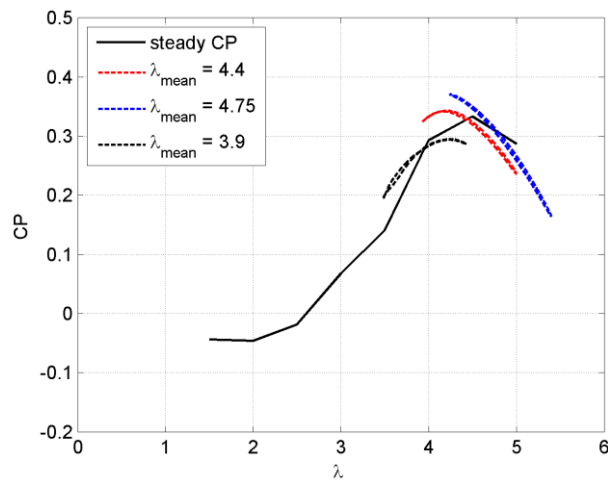
Figure 29. Study on the effect of varying λ_{mean}.

λ_{mean} = 3.9 λ_{mean} = 4.4 λ_{mean} = 4.75
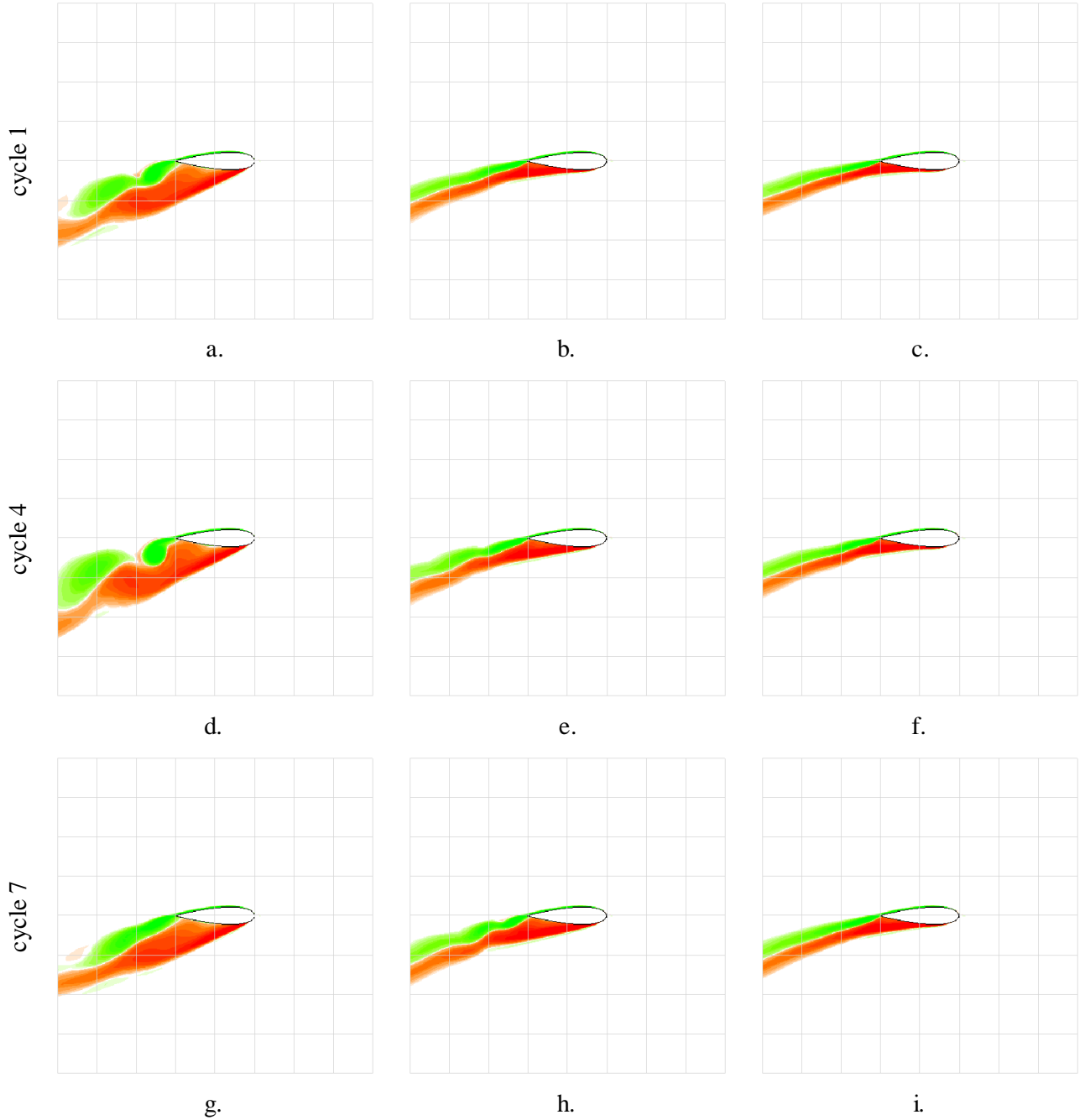
Figure 30. Flow visualisations of selected rotor cycles in the first quarter of the wind cycle showing effects of varying λ_{mean} at $\theta = 130°$.
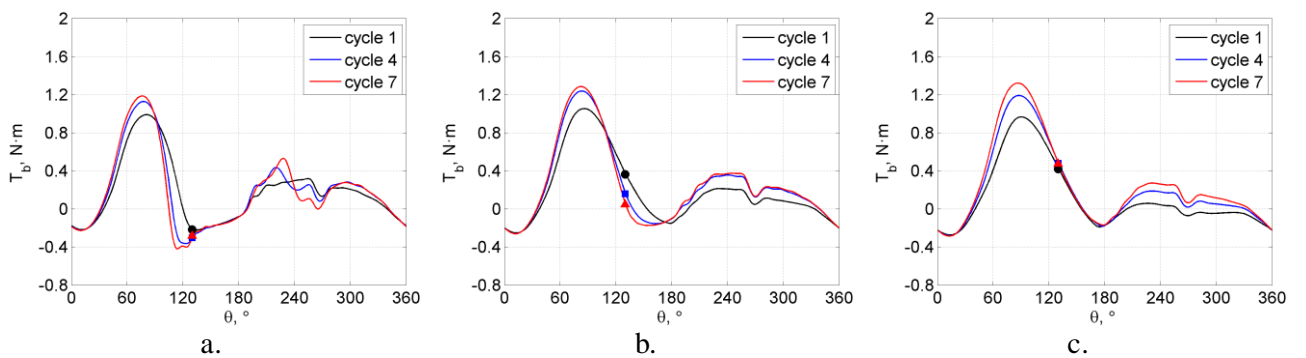
Figure 31. Blade torque T_b plots from three rotor cycles of the different λ_{mean} cases (markers are T_b at $\theta = 130°$): a) $\lambda_{mean} = 3.9$, b) $\lambda_{mean} = 4.4$, c) $\lambda_{mean} = 4.75$.

Figure 30 shows the stalling of one blade at different rotor cycles within the first quarter of the wind cycle as U_∞ rises from 7m/s to 7.84m/s. All images shown are for one azimuth position, $\theta = 130°$. A most obvious observation of the images is the very deep stall on the blade for the $\lambda_{mean} = 3.9$ case (Figure 30a, d & g). There are also large vortex structures shed from the blade leaving a very thick trailing wake. T_b values at this θ are negative and lower than -0.2N·m (Figure 31a). The reference case of $\lambda_{mean} = 4.4$ shows significantly shallower stall than the $\lambda_{mean} = 3.9$ case, with no shed vortices, stall induced by trailing edge separation and a much thinner wake (Figure 30b, e & h). All T_b values are positive, though the T_b for cycle 7 is very low at 0.05N·m (Figure 31b). The third case, where $\lambda_{mean} = 4.75$ shows the shallowest stall of the three with all cycles experiencing trailing edge separation extending only up to the mid chord (Figure 30c, f & i). The wake produced is also thin, with negligible ripple in the tail. All T_b values are positive and greater than 0.4N·m (Figure 31c). Negative T_b generated by the blades is not due to deep stall inducing high drag, but rather the limited α that the blades see affecting the lift generated.

C. Effect of Varying the Fluctuation Amplitude

The effects of the amplitude of fluctuation U_{amp} was investigated by running two simulations at $U_{amp} = \pm7\%$ (±0.49m/s) and $U_{amp} = \pm30\%$ (±2.1m/s) and compared to the reference case of $U_{amp} = \pm12\%$ (±0.84m/s). The variation of λ in time for the three λ_{mean} cases is shown in Figure 32a. From Sec. 6.3.2, the maximum λ of the reference case at $U_{amp} = \pm12\%$ is recorded at 5.0 while the minimum is at 3.93. The peak–to–peak value is for this case is 1.07. The case with the highest $U_{amp} = \pm12\%$ shows the maximum λ has jumped to 6.28 while the minimum is now at 3.38 resulting in a peak–to–peak value of 2.9. A not so extreme behaviour is observed when $U_{amp} = \pm7\%$. The maximum λ is seen to be 4.73 while the minimum is 4.11 giving a peak–to–peak value of 0.62. With a common $\omega = 88$rad/s (840rpm), the peak–to–peak value increases as the U_{amp} increases due to the expanding limits of U_∞. The trend of the CP curves is simple and straightforward. Each half of the wind cycle shows a trough in the CP curve at the point of an extreme value of U_∞ specifically at the quarter cycle ($t = 0.5$s) and three quarter cycle ($t = 1.5$s). From Figure 32b, the CP at quarter cycle falls from 0.34 to 0.32 then to 0.23 with increasing U_{amp} from 7% to 12% then to 30%. A more severe drop in CP is seen at the three quarters cycle where the increasingly negative U_{amp} from -7% to -12% then to -30% cause the CP to plummet from 0.29 to 0.24 down to -0.19. The CP at the start, middle and end of the wind cycle is common for all U_{amp} cases.

U_{amp}	$\pm7\%$	$\pm12\%$	$\pm30\%$
cycle–averaged CP	0.35	0.33	0.25

Table 2. Wind cycle–averaged CP at different U_{amp}.
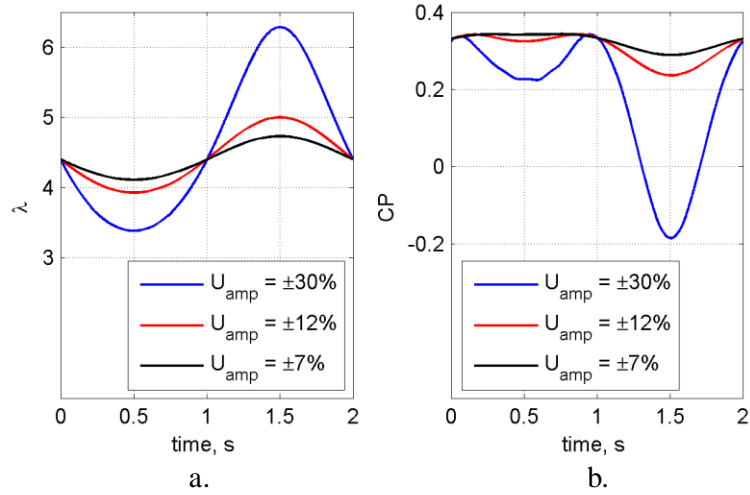
Figure 32. Quasi–steady performance of the VAWT for the different U_{amp} cases:
a) λ vs. time, b) CP vs. time.

The quasi–steady CP curves of all three cases are shown in Figure 33. It can be seen from the figure that the curves are overlapping and essentially coincident, over their ranges of λ. Both the $U_{amp} = \pm7\%$ and $U_{amp} = \pm12\%$ cases trace the quasi–steady CP curve of the $U_{amp} = \pm30\%$ case. Maximum instantaneous CP is 0.34 for all three cases close to $\lambda = 4.2$. The cycle–averaged CP for $U_{amp} = \pm7\%$ is 0.35 while that of $U_{amp} = \pm30\%$ is 0.25. When compared to the reference case cycle–averaged CP of 0.33, a significant drop (24% reduction) in performance is observed for the largest fluctuation amplitude of $U_{amp} = \pm30\%$ while a marginal improvement (6% increase) is seen for the smallest fluctuation amplitude at $U_{amp} = \pm7\%$. At the highest instantaneous λ, the CP registers at −0.19 ($\lambda = 6.29$) for the $U_{amp} = \pm30\%$ case, while it is 0.29 ($\lambda = 4.73$) for the $U_{amp} = \pm7\%$ case. The extent of the quasi–steady CP curve is longer relative to the λ_{mean} point as the wind cycle goes through the second half causing the λ to rise to much higher values versus the first half. The non–linear inverse relationship of U_∞ to λ is the primary factor behind the asymmetric behaviour of the quasi–steady CP.
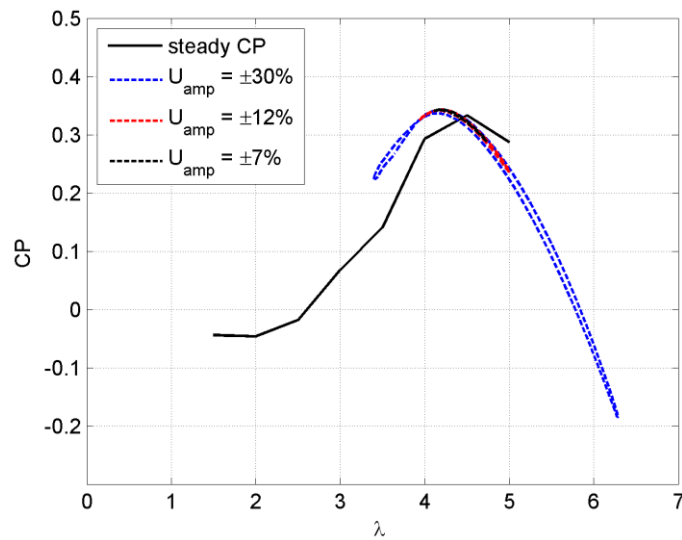
Figure 33. Study on the effect of varying U_{amp}.

$U_{amp} = \pm 7\%$ $U_{amp} = \pm 12\%$ $U_{amp} = \pm 30\%$

a. b. c.

d. e. f.

g. h. i.
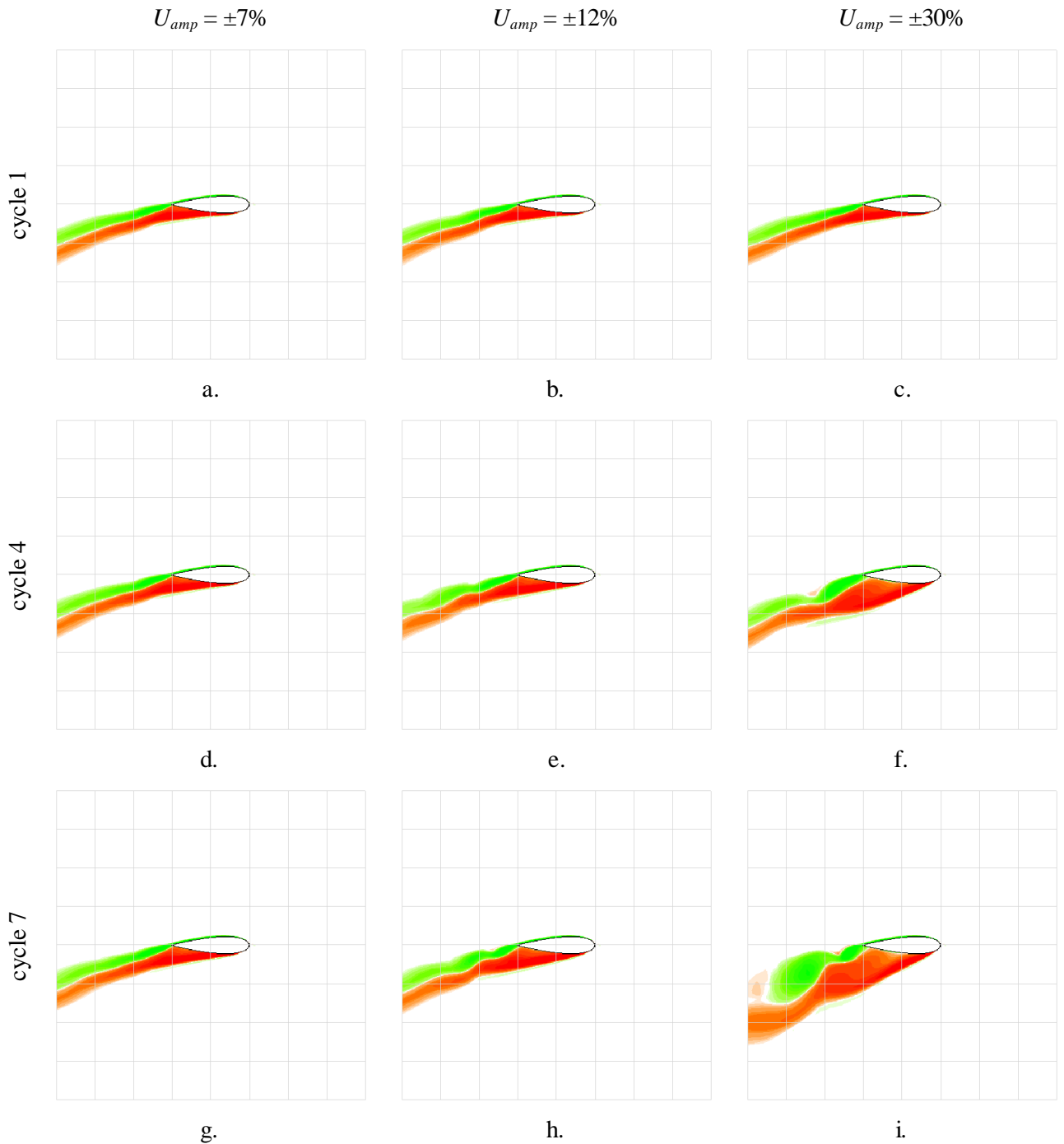
Figure 34. Flow visualisations of selected rotor cycles in the first quarter of the wind cycle showing effects of varying U_{amp} at $\theta = 130°$.

a. b. c.
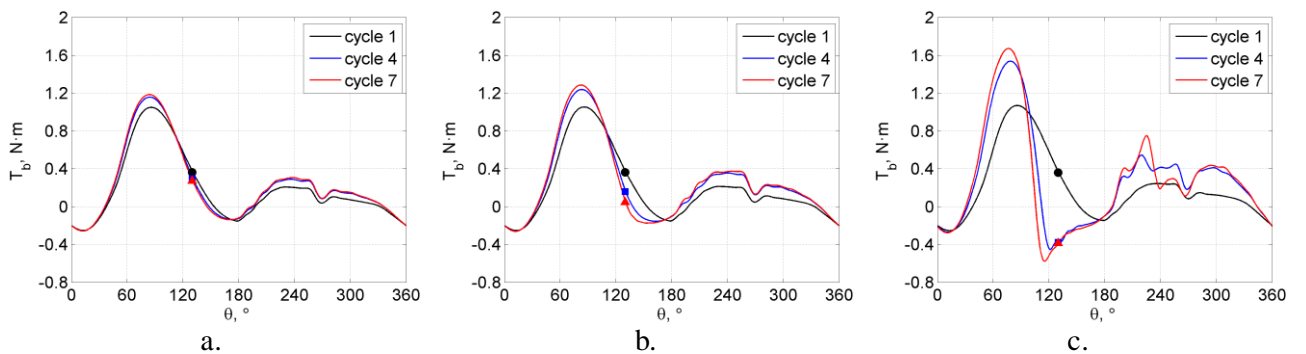
Figure 35. Blade torque T_b plots from three rotor cycles of the different U_{amp} cases (markers are T_b at $\theta = 130°$): a) $U_{amp} = \pm 7\%$, b) $U_{amp} = \pm 12\%$, c) $U_{amp} = \pm 30\%$.

The stalling of one blade at different rotor cycles within the first quarter of the wind cycle is shown in Figure 34. Again, all images shown are for the azimuth position $\theta = 130°$. Starting with the smallest fluctuation amplitude of $U_{amp} = \pm 7\%$, the deepest stall that the blades see is only partial stall from the trailing edge to mid–chord of the blade (Figure 34a, d & g). The wake is thin and there are no visible structures shed from the blade, as well as pronounced wiggling of the wake tail, likely due to the stagnation point staying near or at the trailing edge. The T_b for the three cycles do not differ very much, as shown in Figure 35a where it is 0.36N·m for cycle 1, 0.30N·m for cycle 4, and 0.27N·m for cycle 7. The reference case of $U_{amp} = \pm 12\%$ shows a progressively deepening stall but with no shed vortices and slight wiggling of the trailing edge wake (Figure 34b, e & h). The T_b values at $\theta = 130°$ range from a high 0.36N·m at cycle 1 to a low of 0.05N·m at cycle 7 (Figure 35b). The last case with the largest fluctuation amplitude at $U_{amp} = \pm 30\%$ shows a drastic change in stalling behaviour from shallow stalling at cycle 1 to very deep stalling at cycle 4 and cycle 7 (Figure 34c, f & i). The wake of the blade changes from a thin strip at cycle 1 to a thick and complex wake at cycle 7 that involves alternating pairs of almost chord–sized shed vortices. These huge differences in stalling affect the T_b generated by the blades as Figure 35c shows. Cycle 1 T_b is positive 0.36N·m while cycle 4 and cycle 7 T_b are –0.38N·m and –0.39N·m, respectively.
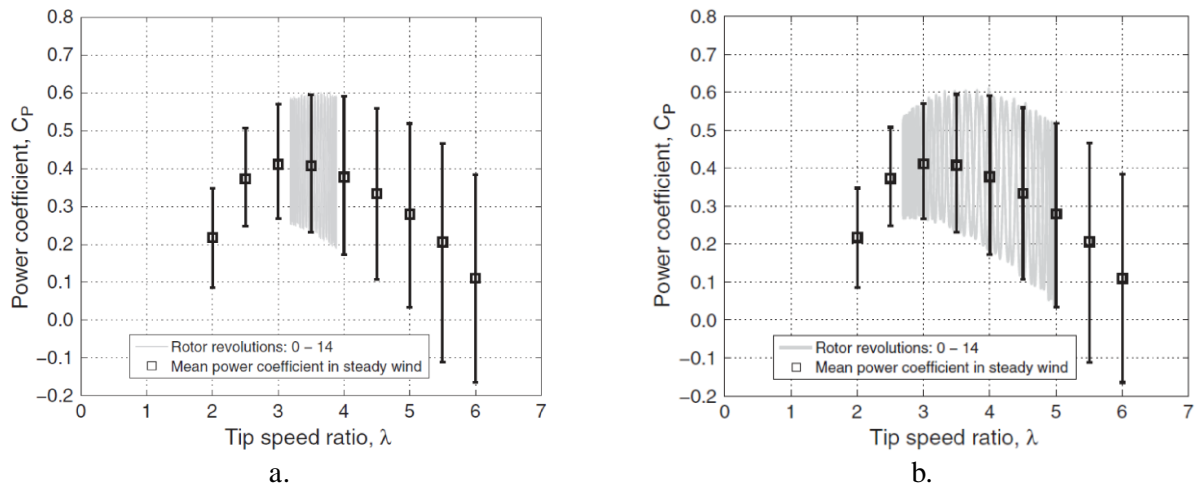
Figure 36. Fluctuation amplitude study by Scheurich and Brown [19]:
a) $U_{amp} = \pm 10\%$, b) $U_{amp} = \pm 30\%$.

Scheurich and Brown [19] conducted a study to investigate the influence of fluctuation amplitude on the overall performance of a 5kW VAWT. Results are presented in Figure 36 and it is apparent in the figures that the behaviour of the unsteady CP almost follows the steady profile as a result of the low reduced gust frequency of $k_g = 0.08$, which requires 14 rotor cycles to complete one wind cycle. The width of the λ range is wider for the $U_{amp} = \pm 30\%$ case than the $U_{amp} = \pm 10\%$ case. What they have found was that the cycle–averaged CP of the straight–bladed VAWT was greatly affected by the magnitude of the U_{amp} and when compared to an 'ideal' case VAWT in steady wind, the cycle–averaged CP dropped to 92% of the ideal CP when $U_{amp} = \pm 30\%$ while the cycle–averaged CP slightly fell to 99% of the ideal CP when $U_{amp} = \pm 10\%$. Kooiman and Tullis [21] determined in their field tests that fluctuation amplitude has a linear effect on the performance of the VAWT and that a $\pm 15\%$ fluctuation only reduced performance by 3.6% from ideal wind conditions.

D. Effect of Varying the Fluctuation Frequency

The effects of the varying fluctuation frequencies f_c was investigated by running two simulations at $f_c = 1Hz$ and $f_c = 2Hz$ and compared to the reference case of $f_c = 0.5Hz$. The variation of λ in time for the three f_c cases is shown in Figure 37a. It is evident that the λ variations of the two higher f_c cases have the same maximum of 5 and minimum of 3.93 as the reference case. The λ plots are seen to be compressed laterally as f_c increases resulting in shorter periods ($t_c = 1s$ for $f_c = 1Hz$, $t_c = 0.5s$ for $f_c = 2Hz$).
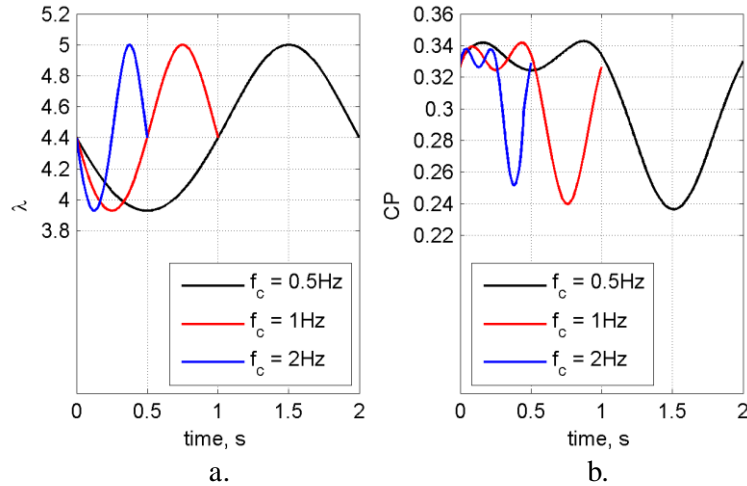
Figure 37. Quasi–steady performance of the VAWT for the different f_c cases:
a) λ vs. time, b) CP vs. time.

U_{amp}	0.5Hz	1Hz	2Hz
cycle–averaged CP	0.33	0.33	0.34

Table 3. Wind cycle–averaged CP at different f_c.

The CP variations between f_c cases show some slight contraction in the peaks and troughs as f_c increases. From Figure 37b, the minimum CP of the reference case is 0.236 while the case with $f_c = 1Hz$ shows a small rise of the minimum to 0.24 and with $f_c = 2Hz$ to 0.25. The maximum CP also changes in decreasing values of 0.343, 0.342, and 0.338 for $f_c = 0.5Hz$, 1Hz, and 2Hz, respectively. At points within the wind cycle where $U_\infty = 7m/s$ (start, midway, and end), the predicted CP for all f_c cases are within the $0.32 - 0.33$ range. These changes are considered to be negligible as the cycle–averaged CP marginally changes from 0.33 for the reference case and the $f_c = 1Hz$ case to 0.34 for the $f_c = 2Hz$ case. This is shown more clearly in the CP–λ plot in Figure 38. The CP curves of the three f_c cases are essentially on top of each other with very little deviation of the highest f_c case in the high λ region. As far as this study is concerned, these differences are insignificant and can be considered negligible within the test parameters that have been investigated.
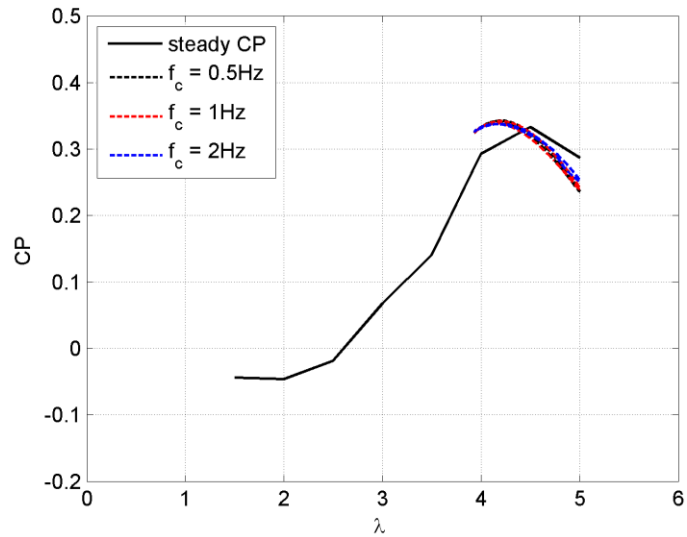
Figure 38. Study on the effect of varying f_c.

a.

b.

c.

d.
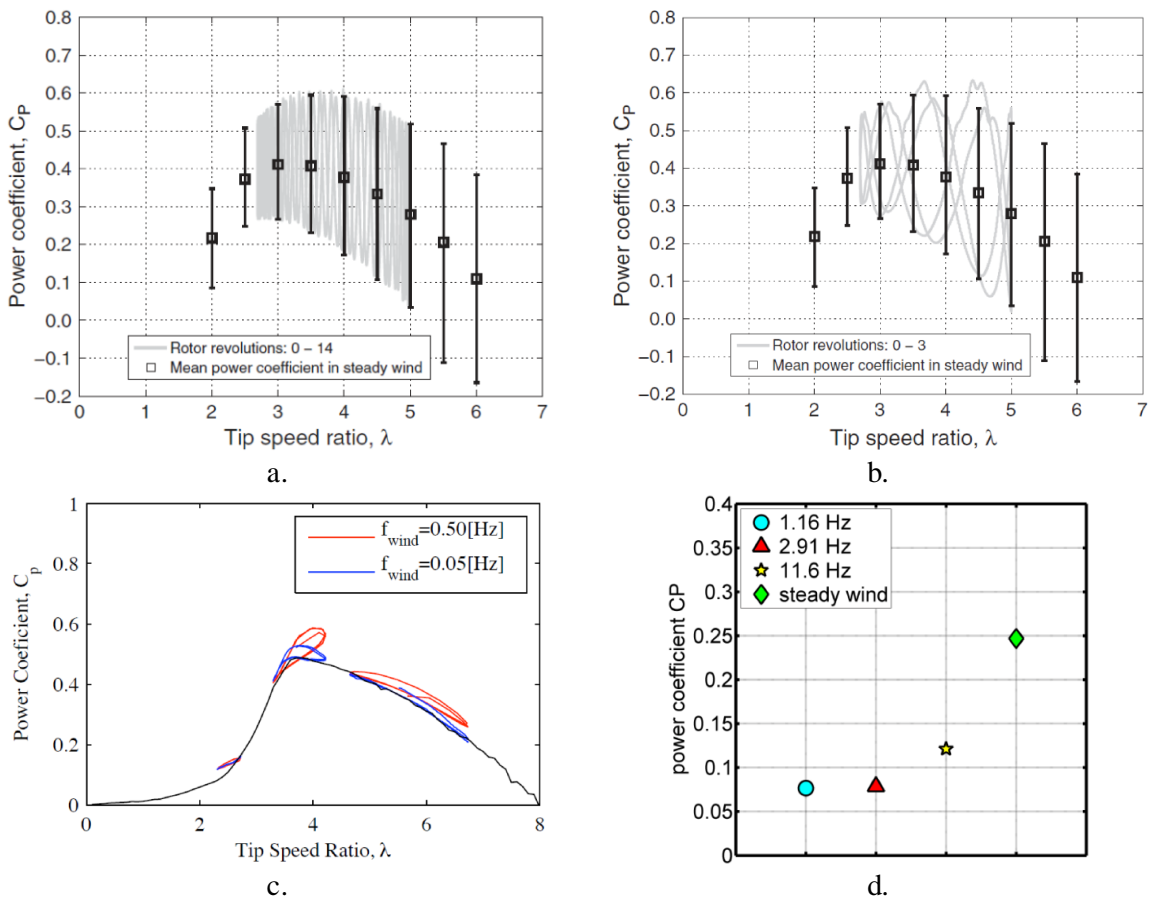
Figure 39. Fluctuation frequency study: a) Scheurich and Brown [19], $f_c = 0.1$Hz,
b) Scheurich and Brown [19], $f_c = 1$Hz; c) McIntosh et al [20], d) Danao and Howell [7].

A study on the effects of fluctuation frequency was conducted by Scheurich and Brown [19] for fluctuation amplitudes of $\pm 10\%$ and $\pm 30\%$. For each fluctuation amplitude, two f_c's were tested, a low f_c of 0.1Hz and a high f_c of 1Hz. The results for the $U_{amp} = \pm 30\%$ are shown in Figure 39a–b. The most apparent observation is that the unsteady CP of both f_c cases generally fall within the limits of the steady CP performance band. As the higher f_c entails fewer rotor cycles per wind cycle, the resulting plot is less condensed with sparsely crisscrossing unsteady CP lines. Cycle–averaged CP increases by less than 2% when f_c changes from 0.1Hz to

1Hz. At a lower U_{amp} of ±10%, the cycle–averaged CP change is even smaller at less than 1% for the same f_c change from 0.1Hz to 1Hz. In contrast, McIntosh et al [20] present increased performance as f_c rises from 0.05Hz to 0.5Hz, especially at operating conditions near peak performance. Danao and Howell [7] studied the effects of different fluctuating frequencies on a VAWT subjected to unsteady wind with U_{mean} = 6.64m/s, U_{amp} = ±50% and λ_{mean} = 4. All of the cases predict performance degradation under any fluctuation frequency. While the present work shows a 25% drop in cycle–averaged CP for conditions of f_c = 0.5Hz and U_{amp} = ±30%, their data show a 75% drop in cycle–averaged CP when conditions are f_c = 1.16Hz and U_{amp} = ±50%. An even higher and unrealistic f_c = 2.91Hz shows the cycle–averaged CP to be very close to the slower case, thus agreeing to the results of the present work. The case with the highest f_c at 11.6Hz is equal to the rotational frequency of the VAWT and is likely not observable in actual conditions, but results still show a drop in performance by about 50%.

VI. Conclusions

Numerical simulations using RANS–based CFD have been utilised to carry out investigations on the effects of steady and unsteady wind in the performance of a wind tunnel VAWT. Using a validated CFD model, steady wind simulations at U_∞ = 7m/s were conducted and results have shown a typical performance curve prediction for this particular VAWT scale. Within the low λ range, there is a distinct negative trough, with drag–dominated performance consistent to experimental results. Minimum CP is computed to be –0.04 at λ = 2 and positive CP is predicted to be attained at λ's higher than 2.5. Maximum CP is 0.33 at λ^* = 4.5 and a shift in the CFD–predicted CP curve to higher λ's is observed relative to the experimental CP profile. A closer inspection of two λ's reveals the fundamental aerodynamics driving the performance of the VAWT. At λ = 2, the blades experience stalled flow initially from a separation bubble forming at θ = 60° with subsequent shedding of vortices alternately cast from the blade surface until reattachment occurs very much delayed beyond halfway of the rotation. The same delayed reattachment is observed as the blade completes the rotation with partial stall still visible at θ = 330°. At λ = 4, blade stall is only observed in the second quadrant of rotation with the deepest stall seen at θ = 130°. High values of positive blade torque T_b reaching 1N·m are predicted in the upwind while most of the downwind region from θ = 190° to θ = 340° also produce positive performance that contribute to the overall positive CP of just below 0.3.

Unsteady wind simulations revealed a fundamental relationship between instantaneous VAWT CP and Reynolds number. Following the dependency of CP to Reynolds number from experimental data, CFD data shows a CP variation in unsteady wind that cuts across the steady CP curve as wind speed fluctuates. A reference case with U_{mean} = 7m/s, U_{amp} = ±12%, f_c = 0.5Hz and λ_{mean} = 4.4 has shown a wind cycle mean CP of 0.33 that equals the maximum steady wind CP at λ = 4.5. Lift coefficient loops uncover performance characteristics of a blade at different points in the wind cycle that depict the presence of dynamic stall as lift values consistently exceed static stall lift in the upwind region. Increasing wind speed causes the instantaneous λ to fall which leads to higher effective α and deeper stalling on the blades. Stalled flow and rapid 'pitch down' motion of the blade induce hysteresis loops in both lift and drag. However, CP–λ loops do

not show any hysteresis due to the quasi–steady effect of the very slow fluctuating wind relative to VAWT ω. Increasing wind speeds have more effect on the tangential component of lift than on drag, which helps improve the performance of the VAWT. Decreasing wind speeds limit the perceived α seen by the blades to near static stall thus reducing the positive effect of dynamic stall on lift generation.

Three cases of different λ_{mean} were run to study the effects of varying conditions of VAWT operation on the overall CP. The case with the highest $\lambda_{mean} = 4.75$ predict a cycle–averaged CP = 0.35 that is marginally higher than the peak steady wind CP of 0.33. In both the reference case with $\lambda_{mean} = 4.4$ and the higher λ_{mean} case, the quasi–steady CP is seen to increase as the wind speed rises. On the other hand, the case with $\lambda_{mean} = 3.9$ behaves differently with falling quasi–steady CP as the wind speed increases. All three cases predict cycle–averaged CPs that are close to steady wind performance at λ's corresponding to the λ_{mean} of each case. Maximum quasi–steady CP is observed to occur at $\lambda = 4.2$ for all cases.

The effects of varying amplitudes of fluctuation were studied by conducting unsteady wind simulations at U_{amp} of $\pm7\%$, $\pm12\%$ and $\pm30\%$. As the magnitude of U_{amp} is increased, a biased detrimental effect is seen in the quasi–steady CP due to the non–linear inverse relationship between U_∞ and λ. Within the second half of the wind cycle where the U_∞ falls below the mean wind speed, the case with $U_{amp} = \pm30\%$ shows the quasi–steady CP drop to –0.19 as λ shoots to above 6. The $U_{amp} = \pm30\%$ case is the worst performing with a cycle–averaged CP of 0.25 while the $U_{amp} = \pm7\%$ case sees an improvement in cycle–averaged CP at 0.35.

Different fluctuation frequencies were also tested and compared to the reference case of $f_c = 0.5$Hz. Results show performance invariance with respect to fluctuation frequency with cycle–averaged CP changes not exceeding 0.01. The case with the highest f_c of 2Hz has a quasi–steady CP curve that almost traces the CP curve of the reference case, despite it being 4 times faster. Cycle–averaged CP predictions are near the steady wind CP maximum of 0.33.

The following conclusions can be derived from the results. When a VAWT operates in periodically fluctuating wind conditions, overall performance slightly improves if the following are satisfied: the mean tip speed ratio is just above the λ of the steady CP maximum, the amplitude of fluctuation is small ($< 10\%$), and the frequency of fluctuation is high (> 1Hz). Operation in λ_{mean} that is lower than λ^* causes the VAWT to run in the λ band with deep stall and vortex shedding, to the detriment of the VAWT CP. Large fluctuations in wind speed causes the VAWT to run in λ conditions that are drag dominated, thus reducing the positive performance of the wind turbine. Within realistic conditions, higher frequencies of fluctuation marginally improve the performance of the VAWT.

References

[1]   "Climate Change 2007: The Physical Science Basis," Technical Report No. AR4, Intergovernmental Panel on Climate Change, Cambridge, United Kingdom and New York, NY, USA.

[2]   Department of Energy Change and Climate. Renewable Energy in 2011, June 2012, Accessed online 31 August 2012, http://www.decc.gov.uk.

[3]   Department of Energy Change and Climate. UK Energy in Brief 2012, July 2012, Accessed online 31 August 2012, http://www.decc.gov.uk.

[4]   Ansys Inc. Fluent 13.0 Documentation, 2010.

[5]   Amet, E., Maitre, T., Pellone, C., and Achard, J. L., 2009, "2d Numerical Simulations of Blade-Vortex Interaction in a Darrieus Turbine," Journal of Fluids Engineering, 131(11), pp. 111103-15.

[6]   Consul, C. A., Willden, R. H. J., Ferrer, E., and Mcculloch, M. D., 2009, "Influence of Solidity on the Performance of a Cross-Flow Turbine " Proceedings of the 8th European Wave and Tidal Energy Conference., Uppsala, Sweden.

[7]   Danao, L. A., and Howell, R., 2012, "Effects on the Performance of Vertical Axis Wind Turbines with Unsteady Wind Inflow: A Numerical Study," 50th AIAA Aerospace Sciences Meeting including the New Horizons Forum and Aerospace Exposition, Nashville, Tennessee.

[8]   Edwards, J., Durrani, N., Howell, R., and Qin, N., 2007, "Wind Tunnel and Numerical Study of a Small Vertical Axis Wind Turbine," 45th AIAA Aerospace Sciences Meeting and Exhibit, Reno, Nevada, USA

[9]   Edwards, J. M., Danao, L. A., and Howell, R. J., 2012, "Novel Experimental Power Curve Determination and Computational Methods for the Performance Analysis of Vertical Axis Wind Turbines," Journal of Solar Energy Engineering, 134(3), pp. 11.

[10]   Hamada, K., Smith, T. C., Durrani, N., Qin, N., and Howell, R., 2008, "Unsteady Flow Simulation and Dynamic Stall around Vertical Axis Wind Turbine Blades," 46th AIAA Aerospaces Sciences Meeting and Exhibit, Reno, Nevada, USA

[11]   Howell, R., Qin, N., Edwards, J., and Durrani, N., February 2010, "Wind Tunnel and Numerical Study of a Small Vertical Axis Wind Turbine," Renewable Energy, 35(2), pp. 412-422.

[12]   Mclaren, K., Tullis, S., and Ziada, S., 2011, "Computational Fluid Dynamics Simulation of the Aerodynamics of a High Solidity, Small-Scale Vertical Axis Wind Turbine," Wind Energy, 15(3), pp. 349-361.

[13]   Raciti Castelli, M., Ardizzon, G., Battisti, L., Benini, E., and Pavesi, G., 2010, "Modeling Strategy and Numerical Validation for a Darrieus Vertical Axis Micro-Wind Turbine," ASME Conference Proceedings, 2010(44441), pp. 409-418.

[14]   Raciti Castelli, M., Englaro, A., and Benini, E., 2011, "The Darrieus Wind Turbine: Proposal for a New Performance Prediction Model Based on Cfd," Energy, 36(8), pp. 4919-4934.

[15]   Simão Ferreira, C. J., Bijl, H., Van Bussel, G., and Van Kuik, G., 2007, "Simulating Dynamic Stall in a 2d Vawt: Modeling Strategy, Verification and Validation with Particle Image Velocimetry Data," Journal of Physics: Conference Series, 75(1), pp. 012023.

[16]   Simão Ferreira, C. J., Van Brussel, G. J. W., and Van Kuik, G., 2007, "2d Cfd Simulation of Dynamic Stall on a Vertical Axis Wind Turbine: Verification and Validation with Piv Measurements," *45th AIAA Aerospace Sciences Meeting and Exhibit*, Reno, Nevada.

[17]   Tullis, S., Fiedler, A., Mclaren, K., and Ziada, S., 2008, "Medium-Solidity Vertical Axis Wind Turbines for Use in Urban Environments," 7th World Wind Energy Conference, St. Lawrence College, Kingston, Ontario.

[18]   Mcintosh, S. C., 2009, "Wind Energy for the Built Environment," Ph.D. thesis, Cambridge University, Cambridge.

[19]   Scheurich, F., and Brown, R. E., 2012, "Modelling the Aerodynamics of Vertical-Axis Wind Turbines in Unsteady Wind Conditions," Wind Energy, pp. 17.

[20]   Mcintosh, S. C., Babinsky, H., and Bertenyi, T., 2008, "Unsteady Power Output of Vertical Axis Wind Turbines Operating within a Fluctuating Free-Stream," 46th AIAA Aerospace Sciences Meeting and Exhibit, Reno, Nevada.

[21]   Kooiman, S. J., and Tullis, S. W., 2010, "Response of a Vertical Axis Wind Turbine to Time Varying Wind Conditions Found within the Urban Environment," Wind Engineering, 34(4), pp. 389-401.